Study of zero-chromaticity in FFAG accelerators

LAGRANGE Jean-Baptiste Henri Raymond

Abstract

Interest on fixed field alternating gradient (FFAG) accelerators has been subject to a great revival in the last decade, because of new needs and thanks to new available technologies, as indicates the increasing number of FFAGs built or under commissioning around the world. Most of them are built so that the chromaticity is suppressed, i.e. the number of betatron oscillations is invariant with the particle energy.

Chromaticity is indeed an essential feature in particle accelerators, since it creates issues of betatron resonance crossing, and limits the momentum range available in the machine. In FFAG rings, an analytical solution of the magnetic field configuration called "scaling" condition is usually used to suppress the chromaticity. It is indeed possible to keep independent of momentum the transverse linearized equations of motion if two conditions are fulfilled. The first one is that the different momentum closed orbits should be photographic enlargements from each other in the median plane. The second one is that the vertical magnetic field in the median plane follows a law in machine radius to the power of k, constant geometrical field index. But this law implies to use circular machines with only one type of cell and constrains the shape of the accelerator.

To overcome this constraint, the application of the scaling condition on a straight FFAG beam line has been considered in this study. It is indeed possible to keep independent of momentum the transverse linearized equations of motion if two equivalent conditions as in the circular case are fulfilled. The first one is the orbit similarity, that is to say the different momentum reference trajectories are a translation of each other in the median plane. The second one is the vertical magnetic field B_z in the median plane should follow

$$B_z = B_{0z} e^{m(x-x_0)} \mathcal{F},$$

with x the horizontal cartesian coordinate, m the normalized field gradient, $\mathcal{F}$ an arbitrary function and $B_{0z} = B_z(x_0)$. This new field law leads to the introduction of insertions in FFAG accelerators, like dispersion suppressors. To confirm and study this new straight scaling field law, an experiment has been done at Kyoto University. A prototype of a straight scaling FFAG cell with this particular magnetic field configuration has been designed and manufactured. The magnetic field has been measured, and horizontal phase

advance of two different energies passing through this prototype cell is quantified. Applications of these new lattice design tools are finally discussed.

Acknowledgments

The present thesis would not have been achieved without the enthusiastic guidance of my supervisor, Professor Yoshiharu Mori. I am deeply grateful for the unique chance he offered me to integrate his team. His devotion and his wise advice were essential all along these years, and allowed me to pursue my own path.

I am also deeply grateful to Dr. Yoshihiro Ishi, Dr. Tomonori Uesugi, Dr. Yasutoshi Kuriyama, Dr. Qin Bin and Dr. Kota Okabe for their great help all along these years. They always had time to answer my questions and correct my mistakes at any moment of the day and night.

I owe my sincere thanks to Professor Sho Ohnuma, who spent several weeks in the laboratory and helped me a lot in the theoretical part of my research.

I thank with all my heart my friends and colleagues Emi Yamakawa, Thomas Planche and Hirofumi Yoshino for the work we have done together, and for their continuous and warm support in the daily life. I do not have enough words to say how much it means to me.

I do not forget Mayumi Mikura, Yuka Ono, Masako Taki and Tomoko Ono for their warm welcome when I arrived in Japan, their kindness that made me feel home, and their vital help to find financial supports.

I wish to express my warm and sincere gratitude to the members of the research team I did not named yet and who all helped me at some point in my research, Prof. Izumi Sakai, Ryotaro Nakano, Yusuke Niwa, Tomoya Minamikawa, Yasuhiro Ito, Tomohiro Suzuki, Shun Oshikawa and Mao Takabatake.

The financial support from the Japanese Ministry of Education (MEXT) is also gratefully acknowledged.

Enfin, en français, je voudrais remercier mes parents, mes grand-parents, ma sœur et mes frères Aurore, Denis, Mathieu et Victor, sans qui je ne serais pas la personne que je suis aujourd'hui.

Contents

Chapter 1

Introduction

1.1 FFAG accelerators

A fixed field alternating gradient (FFAG) accelerator is defined as a circular particle accelerator, with a static guide field, like cyclotrons, and focusing and defocusing elements alternated to provide a strong focusing similar to ordinary synchrotrons. FFAG principle proposal came shortly after the discovery of the alternating gradient focusing [1] in the 1950s, in Japan [2], in USSR [3] and USA [4, 5], independently.

1.1.1 The MURA age

The first FFAG model, Mark II, was built in 1955 by the Midwestern Universities Research Association (MURA) group [6] in the USA. This ring was an electron accelerator, where normal and reversed bends were used to realize the alternating gradient focusing. Another way to perform strong focusing is to use alternating edge focusing, with spiral shape magnets [7], as it was demonstrated with the second electron model built in 1956 [8]. Contrary to the reverse bends that can increase substantially the ring size, spiral FFAG has the advantage to keep small the circumference factor. The third and last model of this age, an electron colliding ring, was built in 1961 [9].

After the MURA age, closed in 1967, FFAG development was paused for about 40 years. Technical issues such as FFAG combined function magnets designs which require finite element magnetic computations, made it difficult to achieve at this time. If cyclotrons benefitted from the spiral geometry developed with FFAGs [5, 4], pulsed synchrotrons were favored over FFAGs for high energy physics.

1.1.2 New needs in particle accelerators

Research in particle accelerators for high energy physics has recently entered a new era. Until the Large Hadron Collider (LHC), the scientific community indeed prospected essentially on the energy frontier to look at finer details of elementary particles, but this interest is fading for technology reasons, and the importance of the beam power has been growing instead these years.

Intense source of secondary particles, such as neutrinos, muons and neutrons, from high-power proton beams are now a priority in several fields. On the one hand, muons can be used in high energy physics as the next generation of lepton-antilepton collider [10]. They can also decay in a storage ring in neutrinos with a well-known flux and flavor, allowing precise experiments on neutrino oscillations [11]. On the other hand, intense neutron sources are essential for accelerator driven sub-critical reactors (ADSR) and for pulsed spallation neutron sources (SNS) [12].

The beam power depends on the final energy, but also on the average beam current. In consequence, a break-through in the beam power frontier requires high energy beam and high repetition rate. Conventional synchrotrons are the best way to achieve high energies, but the repetition rate ($\sim$1 Hz) is too low to attain a high average current. Rapid cycling synchrotrons can compensate this drawback to a certain extent ($\sim$100 Hz) [13], but at an expensive and large power consumption price. Cyclotrons can achieve very large currents with a continuous wave (CW) mode, but have difficulties to reach relativistic energies, due to their isochronism. Even if linear accelerators achieve both high energies and high currents, their cost and power consumption make practical realization difficult.

A solution would be the use of FFAG synchrotrons [14]. They can reach relativistic energies, contrary to cyclotrons, and fixed field leaves them free from magnet ramping issues, unlike pulsed synchrotrons. High repetition rates at high energies can then be reached in such machines, making them a suitable candidate for delivering high power beams. Fast acceleration is also mandatory when accelerating unstable particles, such as muons. Another advantage pushing forward FFAG synchrotron development is their possible huge transverse and longitudinal acceptance, capable of handling very large beams.

FFAGs can also be useful in medical field, since possibility to command

a rapid cycling variable energy would be a great asset for hadrontherapy [15, 16]. It would allow a rapid depth scanning of tumors, for a better efficiency of the treatment, and an increased number of treatable patients.

1.1.3 The rebirth of FFAG

Computation tools played an important role in the recent developments. FFAG magnets are now designed with finite element magnetic software such as TOSCA [17, 18, 19, 20], and non-linear beam dynamics can be studied with step-wise particle tracking codes [21, 22, 23]. Technological developments are also essential in the new rise of FFAGs. High field broad band radio-frequency cavities [24, 25] made it possible to sweep quickly rf frequencies with large rf voltages, and thus enable high repetition rates in proton FFAGs.

FFAGs built in the early age were all electron accelerators, and the world's first proton FFAG synchrotron, POP-FFAG, was commissioned in 2000 [26] at the Japanese high energy accelerator research organization (KEK). A 150 MeV radial sector type ring followed this success and was commissioned at KEK in 2004 [27]. Another step was reached with the building of a full FFAG proton complex made of 3 scaling FFAG rings as a driver for ADSR studies at Kyoto University Research Reactor Institute (KURRI) [28]. Besides, application as a proton driver for a neutrino factory is now considered [29]. Moreover, the production of an effective intense source of neutrons from proton beams is also investigated, with the development and construction of the energy recovering internal target (ERIT) FFAG scheme [30, 31]. The development of a pure and quasi monoenergetic muon source is also carefully studied, which led to the PRISM FFAG ring development [32] and the creation of the PRISM task force [33, 34]. Several FFAG rings were finally designed for hadrontherapy [15, 16].

All these FFAGs are designed to keep transverse focusing invariant with energy. However, it brings strong limitations on the lattice parameters. To get more free parameters, another type of FFAG recently appeared, relaxing on the invariant focusing condition. The first FFAG of this type, the electron model EMMA, is built and under commissioning in Daresbury Laboratory [35, 36, 37]. Yet, the loss of the invariant focusing of this type of FFAG brings its own limitations. Very fast acceleration must be achieved and deterioration of the beam properties are encountered during acceleration.

1.2 Zero-chromaticity

As it is reminded in App. A, the choice of the tune far away from harmful resonances lines is important but it is also essential that the tune does not vary with energy, since it would encounter the crossing of betatron resonances during acceleration. In consequence, the concept of zero-chromaticity is introduced and defined as the invariance of both the horizontal and the vertical tune with respect to the momentum of the particles.

A sufficient condition to obtain the zero-chromaticity in a lattice is to keep independent of momentum the betatron oscillations. Zero-chromatic FFAGs built so far fulfilled this sufficient condition with the so-called "scaling law". As it will be detailed in Chap. 2, besides the orbit similarity, the magnetic field configuration in the mid-plane must follows

$$B_z = B_{0z} \left(\frac{r}{r_0} \right)^k \cdot \mathcal{F}, \tag{1.1}$$

with r the polar coordinate, k the constant geometrical field index, $\mathcal{F}$ an arbitrary function and $B_{0z} = B_z(r_0)$.

However, it is not a necessary condition, since it is possible to keep stable over a certain momentum range the number of oscillations, while these oscillations depend on momentum [38]. But this kind of solution can be done only numerically, and an analytical solution is essential to have a proper understanding of the phenomena at stake.

1.3 Purpose of this study

FFAG accelerators have been the object of a renewed interest in the last decade. Remarkable features make this type of accelerator a good candidate for many applications in several fields. Zero-chromaticity is an essential feature in the machine, since it allows large transverse acceptance and large momentum spread. But zero-chromatic FFAGs built so far are very constrained regarding the transverse motion. They have to be circular rings, with only one type of cell, and no insertions. Insertions could be a great asset in FFAGs, since the different functions could be decoupled in the rings, with a modular system similar to pulsed synchrotrons.

Preliminary studies on insertions in FFAGs have been done in the past [39, 40], but none was done so that FFAG accelerators could be zero-chromatic with no overall bend.

The purpose of this study is to examine straight zero-chromatic FFAGs, allowing transverse focusing in this type of accelerator. Matching with arc sections is also investigated. It opens a new range of applications for FFAG accelerators, that is then studied.

1.4 Organization of the study

An analytical development of the invariance of the betatron oscillations with momentum in circular FFAG and in straight FFAG is described in the chapter 2. Induced properties are then presented, with the introduction of insertions in FFAG accelerators, like dispersion suppressors. The straight scaling FFAG experiment procedure is then developed in chapter 3, and the measured results are analyzed. Some practical applications of these new lattice design tools are finally discussed in chapter 4. Summary is presented in chapter 5, and conclusion is finally discussed in chapter 6.

Chapter 2
Theory

The configuration of the static magnetic field of the FFAGs is determined in this section in order to keep invariant the betatron oscillations with respect to momentum. This development is based on the orbit theory, like in Ref. [4], where characteristics of a distinctive accelerator are specified by its equilibrium orbits. However, the parameters ϵ and η used in Refs. [4, 41] have a physical meaning difficult to comprehend, and a new approach based on geometrical considerations is developed.

2.1 Circular case

2.1.1 Geometrical specifications

The study is restrained to the case where at any momentum p corresponds a unique closed orbit lying in the median plane, and never crossing another closed orbit. Each closed orbit is then represented in cylindrical coordinates (r, θ, z) by

$$\begin{cases} r = r_{co}(\theta, p), \\ z = 0, \end{cases} \tag{2.1}$$

and is specified by its equivalent radius R

$$R = \frac{1}{2\pi} \oint ds, \tag{2.2}$$

with s the abscissa along the closed orbit. The corresponding azimuthal coordinate Θ is next defined as

$$s = R\Theta. \tag{2.3}$$

Since the different closed orbits never cross each other, they correspond to a unique R, and uniqueness of the closed orbit for a given momentum gives that any couple (r, θ) is related to a unique couple (R, Θ) and vice versa. (R, Θ, z) is then a possible system of coordinates.

2.1.2 Betatron oscillations

The motion of a charged particle with a given momentum is described by the following linearized equations for small amplitudes [1]

$$\begin{cases} \dfrac{d^2x}{ds^2} + \dfrac{1-n}{\rho^2}x = 0, & \text{(a)} \\ \dfrac{d^2z}{ds^2} + \dfrac{n}{\rho^2}z = 0, & \text{(b)} \end{cases} \tag{2.4}$$

in the local curvilinear coordinate system (x, s, z). The field index n is defined as:

$$n = -\frac{\rho}{B}\left(\frac{\partial B}{\partial x}\right)_{\perp}, \tag{2.5}$$

with B the vertical component of the magnetic field. The symbol $\perp$ means that the partial derivative is done in the machine mid-plane perpendicularly to the closed orbit, and evaluated at $x = 0$.

The linearized equations of motion can be rewritten in the coordinate system (x, Θ, z):

$$\begin{cases} \dfrac{d^2x}{d\Theta^2} + \dfrac{R^2}{\rho^2}(1-n)x = 0, & \text{(a)} \\ \dfrac{d^2z}{d\Theta^2} + \dfrac{R^2}{\rho^2}nz = 0. & \text{(b)} \end{cases} \tag{2.6}$$

The invariance of the betatron oscillations with respect to momentum means that Eq. 2.6(a) and Eq. 2.6(b) are independent of momentum. A necessary and sufficient condition of the invariance of the betatron oscillations along the curves $\Theta = const.$ can thus be given by:

$$\begin{cases} \left(\dfrac{\partial(R/\rho)}{\partial p}\right)_{\Theta} = 0, & \text{(a)} \\ \left(\dfrac{\partial n}{\partial p}\right)_{\Theta} = 0. & \text{(b)} \end{cases} \tag{2.7}$$

This is a sufficient condition of zero-chromaticity. From Eq. 2.7(a), the similarity of the closed orbits is thus a necessary condition for the invariance of the betatron oscillations. Eq. 2.7(a) can actually be integrated as

$$\rho(p, \Theta) = R(p) \cdot f(\Theta), \tag{2.8}$$

with f a function independent of momentum. Furthermore, Eq. 2.8 is equivalent to:

$$r_{co}(p, \Theta) = R(p) \cdot g(\Theta). \tag{2.9}$$

The function g is independent of momentum and can be seen as the "shape term", common of all the closed orbits, while R is the "scaling term".

We now focus on the condition given in Eq. 2.7(b), i.e. the invariance of the field index n with momentum. If we derive in the median plane the equation $p = qB\rho$, for a particle of momentum p and charge q, with respect to x and at $x = 0$, we have:

$$B\left(\frac{\partial \rho}{\partial x}\right)_{\perp} + \rho\left(\frac{\partial B}{\partial x}\right)_{\perp} = \frac{1}{q}\left(\frac{\partial p}{\partial x}\right)_{\perp}. \tag{2.10}$$

Here again, the symbol $\perp$ means that the partial derivative is done in the machine mid-plane perpendicularly to the closed orbit, and evaluated at $x = 0$. The field index n can thus be rewritten as:

$$n = \left(\frac{\partial \rho}{\partial x}\right)_{\perp} - \frac{\rho}{p}\left(\frac{\partial p}{\partial x}\right)_{\perp}. \tag{2.11}$$

We then express the field index n in the system of coordinates (R, Θ, z):

$$n = \left(\frac{\partial R}{\partial x}\right)_{\perp}\left[R\left(\frac{\partial(\rho/R)}{\partial R}\right)_{\Theta} - \frac{\rho}{R}k\right] + \left(\frac{\partial \Theta}{\partial x}\right)_{\perp} R\left(\frac{\partial(\rho/R)}{\partial \Theta}\right)_{R}, \tag{2.12}$$

with k a factor defined by:

$$k(R, \Theta) = \frac{R}{p}\frac{dp}{dR} - 1. \tag{2.13}$$

The parameter k can be rewritten using the mean magnetic field $\bar{B} = p/(qR)$ as the mean geometrical field index:

$$k = \frac{R}{\bar{B}}\frac{d\bar{B}}{dR}. \tag{2.14}$$

The geometrical field index k is also independent of Θ, since momentum and Θ are independent of each other.

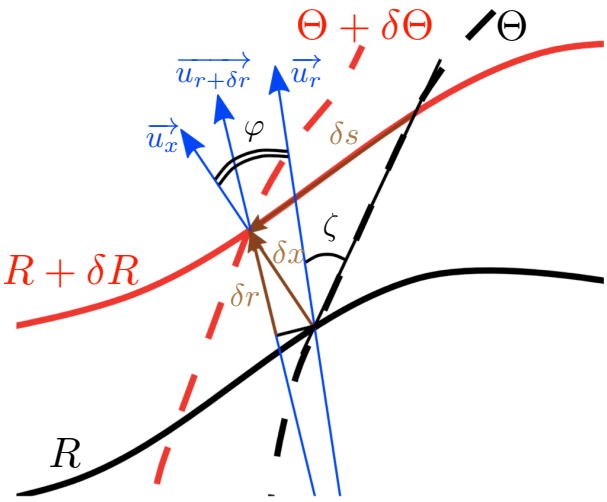

Figure 2.1: Geometrical considerations for the circular case.

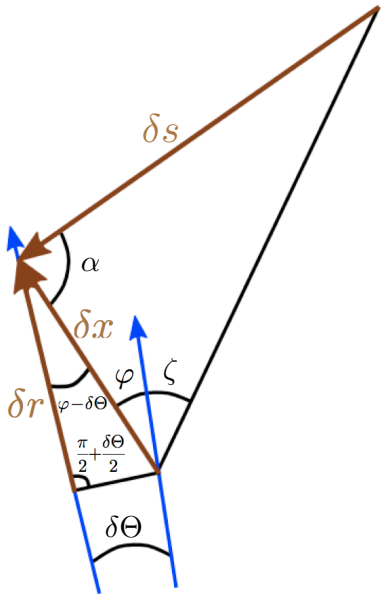

Figure 2.2: Geometrical considerations, zoom of Fig. 2.1.

2.1.3 Geometrical considerations

We now clarify the differential terms of Eq. 2.12 with geometrical considerations. The condition given in Eq. 2.7(a) implies that

$$\begin{cases} \left(\dfrac{\partial(\rho/R)}{\partial R}\right)_{\Theta} = 0, \\ \rho/R = f(\Theta), \\ \left(\dfrac{\partial(\rho/R)}{\partial \Theta}\right)_{R} = \dfrac{df}{d\Theta}. \end{cases} \tag{2.15}$$

With the parameters defined in Fig. 2.1 and its zoom Fig. 2.2, we have the expression

$$\frac{\delta s}{\delta x} = \frac{\sin(\zeta+\varphi)}{\sin(\alpha+\zeta+\varphi)}. \tag{2.16}$$

We also have from Eq. 2.2

$$\frac{\delta r}{\delta x} = \frac{\cos(\varphi - \frac{\delta\Theta}{2})}{\cos\frac{\delta\Theta}{2}}. \tag{2.17}$$

Passing to the limit $\delta x \to 0$, we get from Eq. 2.16 and Eq. 2.17:

$$\begin{cases} \left(\dfrac{\partial s}{\partial x}\right)_{\perp} = R\left(\dfrac{\partial\Theta}{\partial x}\right)_{\perp} = \tan(\varphi+\zeta), \\ \left(\dfrac{\partial r}{\partial x}\right)_{\perp} = \cos\varphi. \end{cases} \tag{2.18}$$

In addition, a first-order development of Eq. 2.9 gives:

$$\begin{aligned} \delta r &= \delta R \cdot g(\Theta) + R\delta\Theta\left(\frac{g(\Theta+\delta\Theta)-g(\Theta)}{\delta\Theta}\right) \\ &= \delta R \cdot g(\Theta) + \delta r \cdot \frac{\delta x}{\delta r}\cdot\frac{\delta s}{\delta x}\left(\frac{g(\Theta+\delta\Theta)-g(\Theta)}{\delta\Theta}\right). \end{aligned} \tag{2.19}$$

Again, passing to the limit $\delta x \to 0$ leads to

$$\left(\frac{\partial R}{\partial r}\right)_{\perp} = \frac{1}{g(\Theta)}\left(1 - \frac{dg}{d\Theta}\frac{\tan(\zeta+\varphi)}{\cos\varphi}\right). \tag{2.20}$$

On the other hand, we also have from Fig. 2.3

$$\left(\frac{\partial r}{\partial\Theta}\right)_{R} = -R\sin\varphi, \tag{2.21}$$

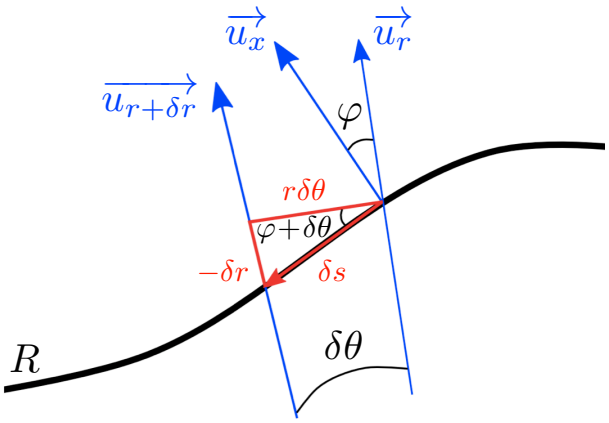

Figure 2.3: Geometrical considerations around one closed orbit.

leading to

$$\frac{dg}{d\Theta} = -\sin\varphi. \tag{2.22}$$

Starting from

$$\left(\frac{\partial R}{\partial x}\right)_{\perp} = \left(\frac{\partial R}{\partial r}\right)_{\perp} \cdot \left(\frac{\partial r}{\partial x}\right)_{\perp}, \tag{2.23}$$

we can finally express $\left(\frac{\partial R}{\partial x}\right)_{\perp}$ of Eq. 2.12 by

$$\left(\frac{\partial R}{\partial x}\right)_{\perp} = \frac{1}{g(\Theta)}\left(\cos\varphi + \sin\varphi \cdot \tan\left(\zeta+\varphi\right)\right). \tag{2.24}$$

The geometrical similarity gives that the angle φ is independent of momentum along the curves $\Theta = const$. In consequence, we use the expressions given in Eq. 2.15 and in Eq. 2.24, and replace them in Eq. 2.12:

$$n = -\frac{f(\Theta)}{g(\Theta)}\left(\cos\varphi + \sin\varphi\tan(\zeta+\varphi)\right)\cdot k + \frac{df}{d\Theta}\tan(\zeta+\varphi). \tag{2.25}$$

From Eq. 2.7(b), n must be independent of momentum along the curves $\Theta = const.$, we can thus express the parameter $k(R,\Theta)$ with Eq. 2.25

$$k(R) = k_1(\Theta) + k_2(\Theta)\tan\zeta(R,\Theta), \tag{2.26}$$

with k_1 and k_2 parameters independent of R:

$$\begin{cases} k_1 = \dfrac{g}{f}\left(\dfrac{df}{d\Theta}\sin\varphi - n\cos\varphi\right) \\ k_2 = \dfrac{g}{f}\left(\dfrac{df}{d\Theta}\cos\varphi + n\sin\varphi\right) \end{cases}. \tag{2.27}$$

The similarity also provides that ζ is independent of Θ. We can now integrate Eq. 2.13 with the help of Eq. 2.26:

$$p = p_0\left(\frac{R}{R_0}\right)^{k_1+1} \cdot e^{\left[k_2\int_{R_0}^{R}\frac{\tan\zeta(R)}{R}dR\right]}, \tag{2.28}$$

with $R_0 = R(p_0)$.

The magnetic field distribution in the median plane then follows:

$$B(R,\Theta) = B_0\left(\frac{R}{R_0}\right)^{k_1} \cdot e^{\left[k_2\int_{R_0}^{R}\frac{\tan\zeta(R)}{R}dR\right]} \cdot \mathcal{F}(\Theta), \tag{2.29}$$

with $B_0 = B(R_0)$ and $\mathcal{F}$ a function independent of momentum.

Concerning the curves $\Theta = const.$, they must be chosen continuous and at least two times differentiable. Their variation in θ must also fulfill the condition that the closed orbits never cross each other. Once the curve $\Theta = 0$ is chosen, the similarity provides that every curve $\Theta = const.$ follows the same law up to a constant.

2.1.4 Radial case

The angle ζ can be chosen null, if the curves $\Theta = const.$ are radial lines (see Fig. 2.4): In this case, $k = k_1$, and the momentum follows:

$$p = p_0\left(\frac{R}{R_0}\right)^{k_1+1} = p_0\left(\frac{R}{R_0}\right)^{k+1}. \tag{2.30}$$

Furthermore, it would be interesting to write this expression in polar coordinates. Since we have from Eq. 2.9

$$\frac{R}{R_0} = \frac{r_{co}(\Theta,p)}{r_{co}(\Theta,p_0)}, \tag{2.31}$$

we can conclude that

$$r_{co}(\Theta,p) = r_{co}(\Theta,p_0)\left(\frac{p}{p_0}\right)^{\frac{1}{k+1}}. \tag{2.32}$$

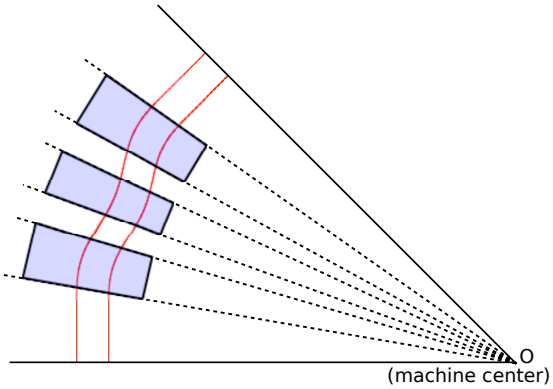

Figure 2.4: Radial case.

The magnetic field distribution follows in the polar coordinates

$$B(r,\theta) = B_0 \left(\frac{r}{r_0}\right)^k \cdot \mathcal{F}(\theta). \tag{2.33}$$

2.1.5 Spiral case

The angle ζ can also be chosen non zero and independent of radius, if the curves $\Theta = const.$ follow a logarithmic spiral (see Fig. 2.5):

$$\theta_{\Theta=const.}(r) = \tan\zeta \cdot \ln\left(\frac{r}{r_0}\right) + \theta_{\Theta=const.,0}, \tag{2.34}$$

with $\theta_{\Theta=const.,0} = \theta_{\Theta=const.}(r_0)$. If ζ is constant, $k = k_1 + k_2 \tan\zeta$ is also constant, and the momentum follows:

$$p = p_0 \left(\frac{R}{R_0}\right)^{k_1+1+k_2\tan\zeta} = p_0 \left(\frac{R}{R_0}\right)^{k+1}, \tag{2.35}$$

Furthermore, in the same way than in radial case, we can express it in polar coordinates

$$r_{co}(\Theta,p) = r_{co}(\Theta,p_0)\left(\frac{p}{p_0}\right)^{\frac{1}{k+1}}. \tag{2.36}$$

The magnetic field distribution follows in polar coordinates

$$B(r,\theta) = B_0 \left(\frac{r}{r_0}\right)^k \cdot \mathcal{F}(\theta - \tan\zeta \ln\frac{r}{r_0}). \tag{2.37}$$

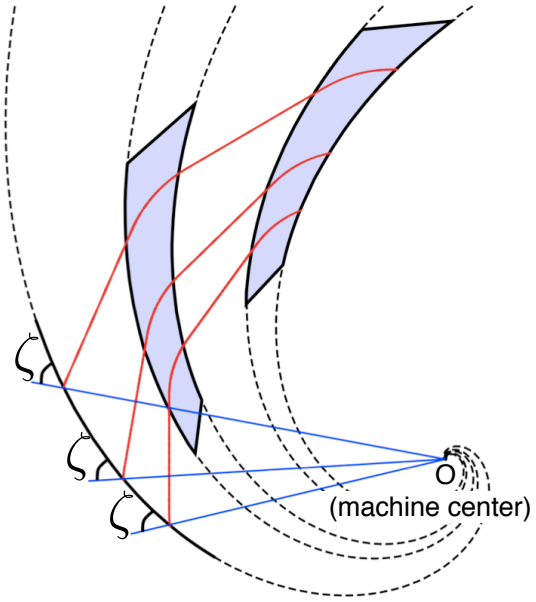

Figure 2.5: Spiral case.

As a remark, the radial case can be seen as the limit of the spiral case, with the spiral angle set to zero.

This field law, so-called "scaling" law, is widely used in FFAG accelerators. It has been verified and studied by experiments in the MURA age. FFAGs are nowadays designed with the help of step-wise tracking codes such as Zgoubi [21] with the "FFAG" procedure and the Runge-Kutta-based code developed at Kyoto University Research Reactor Institute [23] and described in App. B. These codes are cross-checked with experiments through different projects like RACCAM [15, 20].

2.2 Straight case

It is also possible to create FFAGs with no overall bend. The study to have invariance of the betatron oscillations for any momentum is built on the same scheme than for the circular case.

2.2.1 Geometrical specifications

While in circular elements, the concept of closed orbit is obvious, the corresponding notion of reference trajectory in straight elements has to be defined first. A reference trajectory of a straight periodic cell is a trajectory followed by a particle whose coordinates, i.e. angle and position, are the same at the entrance and at the exit of the cell.

In the same way than in circular elements, the study is restrained to the case where at any momentum p corresponds a unique reference trajectory lying in the median plane, and never crossing another reference trajectory. Each reference trajectory is then represented in cartesian coordinates (X, Y, z) by

$$\begin{cases} X = X_{co}(Y, p), \\ z = 0, \end{cases} \tag{2.38}$$

and is specified by its average abscissa χ:

$$\chi = \frac{1}{T} \int_T X_{co}(s) ds, \tag{2.39}$$

with T the period of the straight section and s the abscissa along the closed orbit.

2.2.2 Betatron oscillations

From the linearized equations of motion Eqs. 2.4, a necessary and sufficient condition of the invariance of the betatron oscillations along the curves $s = const.$ is

$$\begin{cases} \left(\dfrac{\partial \rho}{\partial p}\right)_s = 0, & \text{(a)} \\ \left(\dfrac{\partial n}{\partial p}\right)_s = 0, & \text{(b)} \end{cases} \tag{2.40}$$

From Eq. 2.40(a), since the curvature radius ρ does not depend on momentum, the similarity of the reference trajectories is a necessary condition for the invariance of the betatron oscillations. It leads to

$$X_{co}(p, s) = \chi(p) + g(s), \tag{2.41}$$

where g is independent of momentum and can be seen as the "shape term", common of all the reference trajectories, while χ is the "translation term".

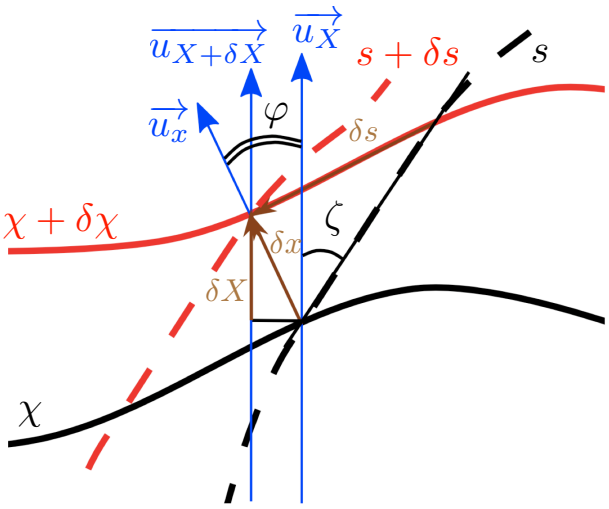

Figure 2.6: Geometrical considerations in the straight case.

We now focus on the condition given in Eq. 2.40(b), i.e. the invariance of the field index n with momentum. Starting from Eq. 2.11, the field index n can be expressed in the coordinates (χ, s, z):

$$n = \left(\frac{\partial\chi}{\partial x}\right)_{\perp}\left[\left(\frac{\partial\rho}{\partial\chi}\right)_{s} - \rho m\right] + \left(\frac{\partial s}{\partial x}\right)_{\perp}\left(\frac{\partial\rho}{\partial s}\right)_{\chi}, \tag{2.42}$$

with m a parameter defined by:

$$m(\chi, s) = \frac{1}{p}\frac{dp}{d\chi}. \tag{2.43}$$

The parameter m can be rewritten with the magnetic field B as the normalized field gradient

$$m = \frac{1}{B}\frac{dB}{d\chi}. \tag{2.44}$$

The normalized field gradient m is independent of s, since the momentum is independent of s.

2.2.3 Geometrical considerations

We now clarify the different terms of Eq. 2.42 with geometrical considerations. Since ρ does not depend on momentum, it does not depend on χ

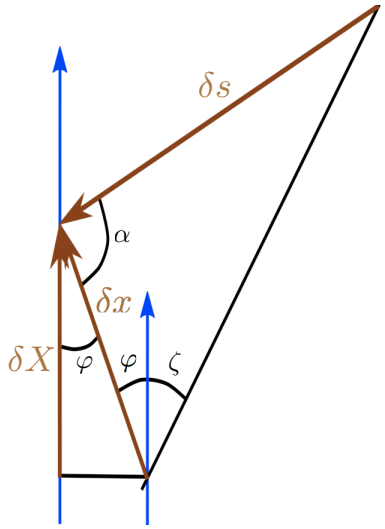

Figure 2.7: Geometrical considerations, zoom of Fig. 2.6.

either:

$$\begin{cases} \left(\dfrac{\partial \rho}{\partial \chi}\right)_s = 0, \\ \left(\dfrac{\partial \rho}{\partial s}\right)_\chi = \dfrac{d\rho}{ds}. \end{cases} \tag{2.45}$$

With the parameters defined in Fig. 2.6 and its zoom Fig. 2.7, we have the expression

$$\frac{\delta s}{\delta x} = \frac{\sin(\zeta + \varphi)}{\sin(\alpha + \zeta + \varphi)}. \tag{2.46}$$

From Fig. 2.7, we also have

$$\frac{\delta X}{\delta x} = \cos\varphi. \tag{2.47}$$

Passing to the limit $\delta x \to 0$, we get from Eq. 2.46 and Eq. 2.47

$$\begin{cases} \left(\dfrac{\partial s}{\partial x}\right)_\perp = \tan(\varphi + \zeta), \\ \left(\dfrac{\partial X}{\partial x}\right)_\perp = \cos\varphi. \end{cases} \tag{2.48}$$

In addition, a first-order development of Eq. 2.41 gives

$$\begin{aligned} \delta X &= \delta\chi + \delta s \left(\frac{g(s+\delta s) - g(s)}{\delta s}\right) \\ &= \delta\chi + \delta X \cdot \frac{\delta x}{\delta X} \cdot \frac{\delta s}{\delta x} \left(\frac{g(s+\delta s) - g(s)}{\delta s}\right). \end{aligned} \tag{2.49}$$

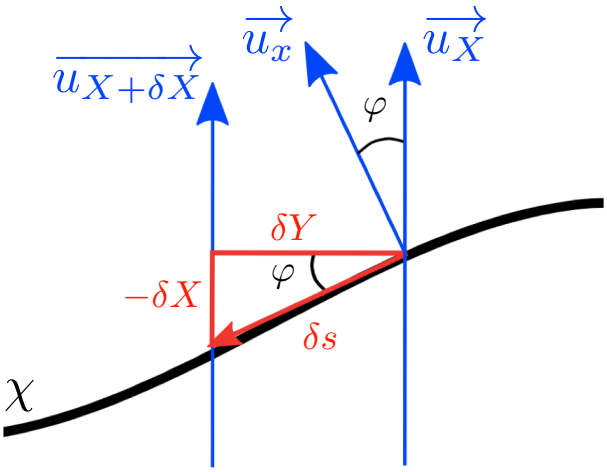

Figure 2.8: Geometrical considerations around one closed orbit.

Passing to the limit $\delta x \to 0$, we deduce from Eq. 2.49

$$\left(\frac{\partial \chi}{\partial X}\right)_{\perp} = 1 - \frac{dg}{ds}\frac{\tan(\zeta+\varphi)}{\cos\varphi}. \tag{2.50}$$

On the other hand, we also have from Fig. 2.8

$$\frac{dX}{ds} = \frac{dg}{ds} = -\sin\varphi. \tag{2.51}$$

Starting from

$$\left(\frac{\partial \chi}{\partial x}\right)_{\perp} = \left(\frac{\partial \chi}{\partial X}\right)_{\perp} \cdot \left(\frac{\partial X}{\partial x}\right)_{\perp}, \tag{2.52}$$

we can finally express $\left(\frac{\partial \chi}{\partial x}\right)_{\perp}$ of Eq. 2.42

$$\left(\frac{\partial \chi}{\partial x}\right)_{\perp} = \cos\varphi + \sin\varphi\tan\left(\zeta+\varphi\right). \tag{2.53}$$

The geometrical similarity gives that the angle φ is independent of momentum along the curves $s = const.$. In consequence, we use the expressions given in Eq. 2.53, Eq. 2.48 and in Eq. 2.45, and replace them in Eq. 2.42:

$$n = -\rho\left(\cos\varphi + \sin\varphi\tan\left(\zeta+\varphi\right)\right)\cdot m + \frac{d\rho}{ds}\tan(\varphi+\zeta). \tag{2.54}$$

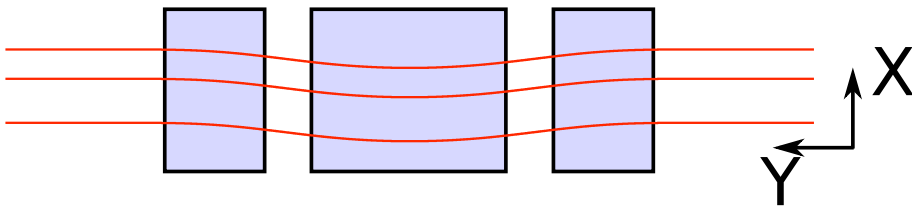

Figure 2.9: Rectangular case.

From Eq. 2.40(b), n must be independent of momentum along the curves $s = const.$ We can thus express the normalized field gradient $m(\chi, s)$ with Eq. 2.54:

$$m(\chi) = m_1(s) + m_2(s) \tan \zeta(\chi, s), \tag{2.55}$$

with m_1 and m_2 parameters independent of momentum:

$$\begin{cases} m_1 = \dfrac{1}{\rho}\left(\dfrac{d\rho}{ds}\sin\varphi - n\cos\varphi\right) \\ m_2 = \dfrac{1}{\rho}\left(\dfrac{d\rho}{ds}\cos\varphi + n\sin\varphi\right) \end{cases}. \tag{2.56}$$

The similarity also provides that ζ is independent of s. Eq. 2.43 can then be integrated:

$$p = p_0 e^{\left[m_1(\chi - \chi_0) + m_2 \int_{\chi_0}^{\chi} \tan\zeta(\chi) d\chi\right]}, \tag{2.57}$$

with $p_0 = p(\chi_0)$.

The magnetic field distribution in the median plane then follows:

$$B(\chi, s) = B_0 e^{\left[m_1(\chi - \chi_0) + m_2 \int_{\chi_0}^{\chi} \tan\zeta(\chi) d\chi\right]} \mathcal{F}(s), \tag{2.58}$$

with $B_0 = B(\chi_0)$, and $\mathcal{F}$ a function independent of momentum.

Concerning the curves $s = const.$, they must be chosen continuous and at least two times differentiable. Their variation in Y must also fulfill the condition that the closed orbits never cross each other. Once the curve $s = 0$ is chosen, the similarity provides that every curve $s = const.$ follows the same law but for a constant.

2.2.4 Rectangular case

The angle ζ can be chosen null, i.e the curves $s = const.$ are straight perpendicular lines, as shown in Fig. 2.9. In this case, the momentum follows

$$p = p_0 e^{m_1(\chi-\chi_0)} = p_0 e^{m(\chi-\chi_0)}. \tag{2.59}$$

Furthermore, it would be interesting to write this expression in cartesian coordinates. Since we have from Eq. 2.41

$$\chi - \chi_0 = X_{co}(s,p) - X_{co}(s,p_0), \tag{2.60}$$

we can conclude that

$$X_{co}(s,p) = X_{co}(s,p_0) + \frac{1}{m} \cdot \ln\left(\frac{p}{p_0}\right). \tag{2.61}$$

The magnetic field distribution follows in cartesian coordinates

$$B(X,Y) = B_0 e^{m(X-X_0)} \mathcal{F}(Y). \tag{2.62}$$

2.2.5 Tilted case

The angle ζ can also be chosen non zero and independent of X, i.e. the curves $s = const.$ follow a tilted straight line (see Fig. 2.10):

$$Y_{s=const.}(X) = (X - X_0)\tan\zeta + Y_{s=const.,0}, \tag{2.63}$$

with $Y_{s=const.,0} = Y_{s=const.}(X_0)$. In this case, $m = m_1 + m_2 \tan\zeta$ is constant, and the momentum follows:

$$p = p_0 e^{(m_1+m_2\tan\zeta)(\chi-\chi_0)} = p_0 e^{m(\chi-\chi_0)} \tag{2.64}$$

Furthermore, in the same way than in rectangular case, we can write this expression in cartesian coordinates

$$X_{co}(s,p) = X_{co}(s,p_0) + \frac{1}{m} \cdot \ln\left(\frac{p}{p_0}\right). \tag{2.65}$$

The magnetic field distribution follows in cartesian coordinates

$$B(X,Y) = B_0 e^{m(X-X_0)} \mathcal{F}(Y - (X - X_0)\tan\zeta). \tag{2.66}$$

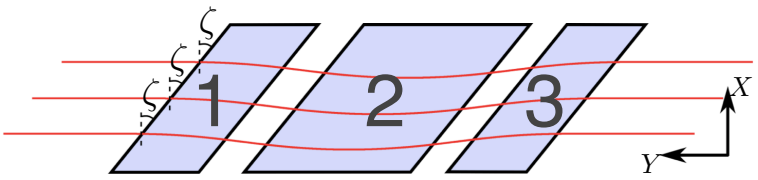

Figure 2.10: tilted case, ζ is constant. It is worth noticing that the magnets 1 and 3 are not identical to keep the same effective path for the particle.

As a remark, the rectangular case can be seen as the limit of the tilted straight case, with the tilted angle set to zero.

This field law is different than in the circular case, and we call it the "straight scaling" law, because the similarity of the trajectories is still a remarkable feature. A new procedure has been developed in the Kyoto University code [23] to study the applications of this new field law, using analytical field modeling in a similar way than in the circular FFAG case, as it is described in App. B. However, an experiment is necessary to cross-check this straight procedure. This is the purpose of Chap. 3.

2.3 Matching of 2 different scaling FFAG cells

To give more freedom to the lattice design in terms of ring shape, it is interesting to consider the combination of different scaling FFAG cells, especially straight and circular [42]. A perfect matching of the curves $s = const.$ between the two different cells can be done only if the circular cell is radial, and if the straight cell is rectangular. However, a first order matching can be done between a spiral cell and a tilted straight cell around an arbitrary momentum if

$$\zeta_{circ.} = \zeta_{str.}, \tag{2.67}$$

with $\zeta_{circ.}$ the angle between the radius and the curves $\Theta = const.$ in the circular cell and $\zeta_{str.}$ the angle between the horizontal abscissa and the curves $s = const.$ in the straight cell.

2.3.1 Periodic dispersion function in scaling FFAG

Since field laws in each section are different, a discontinuity of reference trajectories can occur at the border of the two sections. We first introduce the central related notion of periodic dispersion function $\eta_{circ.}$ and $\eta_{str.}$ for a given momentum p_0 of a circular cell and a straight cell, respectively, and defined as

$$\begin{cases} \eta_{circ.}(p_0) = p_0 \left(\dfrac{\partial r_{co}}{\partial p} \right)_{p_0}, \\ \eta_{str.}(p_0) = p_0 \left(\dfrac{\partial X_{ref}}{\partial p} \right)_{p_0}. \end{cases} \tag{2.68}$$

By applying the definitions described in Eq. 2.68 for scaling FFAGs, we obtain that the periodic dispersion functions $\eta_{circ.}$ and $\eta_{str.}$ for a circular cell and a straight cell, respectively, become

$$\begin{cases} \eta_{circ.}(p_0) = \dfrac{r}{k+1}, \\ \eta_{str.}(p_0) = \dfrac{1}{m}. \end{cases} \tag{2.69}$$

2.3.2 Matching of reference trajectories

In consequence, a combination of a straight scaling FFAG cell and a circular scaling FFAG cell is possible if after matching a given momentum p_0, dispersion is matched with

$$m = \frac{k+1}{R_0}, \tag{2.70}$$

with R_0 the radius of the closed orbit for the momentum p_0 at the border of the cell in the circular section. This matching is done to the first order in $\frac{R-R_0}{R_0}$, with R the radius of the closed orbit for a momentum p at the border of the cell in the circular section. Higher orders effects create a reference trajectory mismatch for momenta other than p_0. By a proper choice of p_0, this mismatch can be minimized for the considered momentum range. An example has been computed by simulating the insertion of straight sections in the 150 MeV FFAG ring of KURRI, for kinetic energies between 20 MeV and 150 MeV. The mismatch x as a function of kinetic energy is presented in Fig. 2.11. This maximum mismatch is around one cm for this case, with a quite small ring. Since the matching is in $\frac{\Delta R}{R_0}$, the mismatch would be smaller for larger rings.

This mismatch induces a reference trajectory distorsion, degrading the zero-chromaticity condition for a large momentum range, especially in lattices where the edge focusing plays an important part.

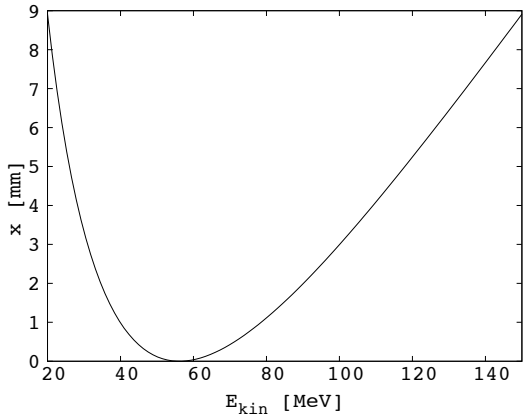

Figure 2.11: Mismatch of reference trajectories between circular cells and straight cells in 150 MeV FFAG ring example.

In the same way, a first-order matching can be used to combine two circular FFAG sections with different radii r_1 and r_2. The dispersion matching condition is kept by adjusting the geometrical field index:

$$\frac{k_1 + 1}{r_1} = \frac{k_2 + 1}{r_2}. \tag{2.71}$$

2.3.3 Matching of linear parameters

Once the reference trajectories are matched, the periodic beta-functions of the cells have also to be matched to limit the amplitude of the betatron oscillations. If a correct matching is not achievable, then an insertion with a phase advance multiple of 180 deg can be done for one of the two different types of cells. This insertion becomes thus transparent, limiting the betatron oscillations.

2.3.4 Dispersion Suppressor principle

In FFAGs, dispersion suppressors can be useful at the end of a transport line where all energies are needed at the same point, or to reduce excursion where rf cavities are set in FFAG rings. The effect of a dispersion suppressor is

indeed to decrease the excursion, i.e. to bring closer the reference trajectories around a matched one. This excursion reduction can even be a complete suppression, as it is presented in the upper part of Fig. 2.12.

A principle of a dispersion suppressor in scaling FFAGs is presented in Fig. 2.12. The components of this scheme are three types of scaling FFAG cells, straight or circular. The area 1 contains FFAG cells with a dispersion η_1 at the border, the area 2, constituting the dispersion suppressor itself, contains FFAG cells with a dispersion η_2 at the borders, and the area 3 contains FFAG cells with a dispersion η_3 at the border. To match the section 1 and 3 with the section 2, the cells of the area 2 must have a phase advance of 180 deg, making this insertion transparent, and the dispersion η_2 has to verify

$$\eta_2 = \frac{\eta_1 + \eta_3}{2}. \tag{2.72}$$

A betatron oscillation is thus induced in the cells of the area 2 for momenta P_1 different than the matched momentum P_0, and allows a matching of the reference trajectories. In the case of a complete dispersion suppression, η_3 is null and $\eta_2 = \eta_1/2$.

This principle is based on the linear theory, so is valid as long as the effect of non-linearities is negligible. The amplitude detuning can break the zero-chromaticity if the difference of dispersion is too large regarding the momentum range.

One solution to overcome this problem is to reduce the dispersion with several dispersion suppressors. An example of 2 dispersion suppressors in cascade is shown in Fig. 2.13. For n dispersion suppressors in cascade to go from an initial dispersion η_{ini} to a final dispersion η_{fin}, the periodic dispersion η_i of the dispersion suppressor number i must then follow

$$\eta_{ini} + (-1)^{n+1}\eta_{fin} = 2\sum_{i=1}^{n}(-1)^{i+1}\eta_i, \tag{2.73}$$

which is a generalized equation of Eq. 2.72.

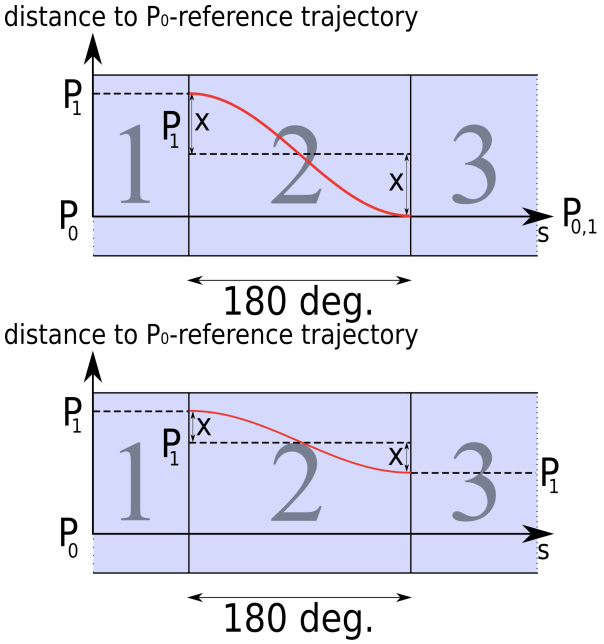

Figure 2.12: Principle of a dispersion suppressor with scaling FFAG cells. The upper scheme shows the case of a complete suppression of the dispersion, the lower one the case of a remaining dispersion after the dispersion suppressor.

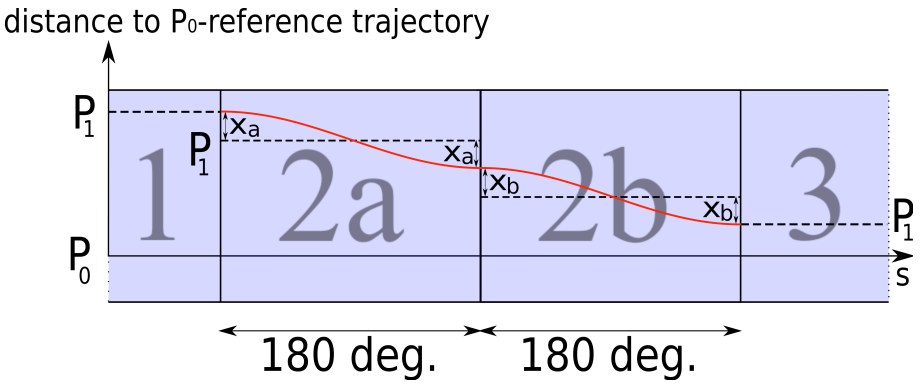

Figure 2.13: Dispersion suppressor in 2 times.

Chapter 3

Experiment

The circular scaling law is well-known and has been verified through experiment, but the straight scaling law is new and has not yet been studied. The experiment described here aims to verify the zero-chromaticity of the straight scaling FFAG law [43, 44].

3.1 Experimental apparatus

3.1.1 Overview

The straight scaling FFAG experiment is performed in the accelerator complex of Kyoto University Research Reactor Institute, in Osaka, Japan.

The main components of this experiment are:

(i) the H^- Linac injector of the 150 MeV FFAG complex, collimated with 2 collimators,

(ii) a Courant Snyder parameters measurement system,

(iii) and the prototype of the straight scaling FFAG cell.

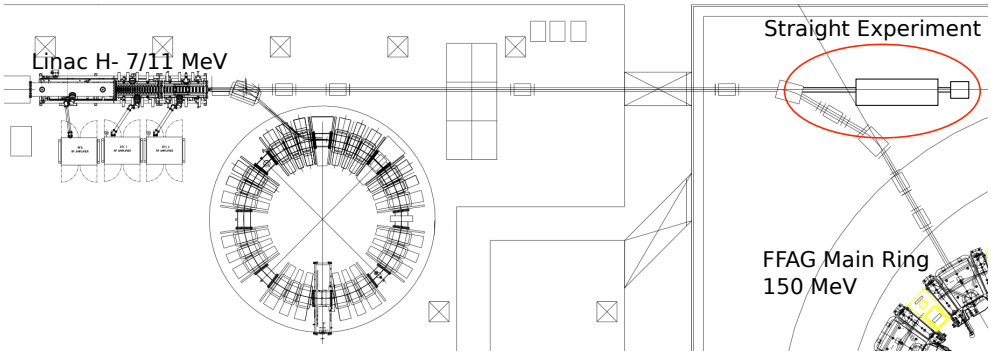

Figure 3.1: Layout of the experiment.

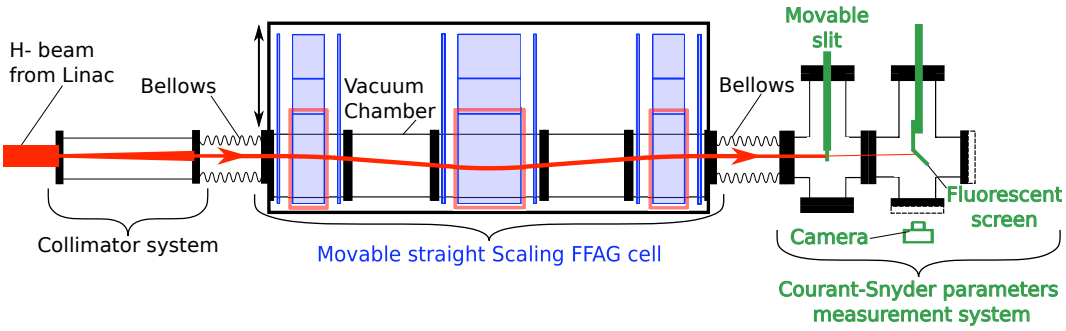

Figure 3.2: Schematic view from above of the experiment.

The prototype of the straight scaling FFAG cell is installed at the end of the straight part of the beam line between the Linac and the FFAG Main Ring, as it is shown in Fig. 3.1. A schematic view of the setup is presented in Fig. 3.2. In this figure, the reference trajectory of the particles is plotted in red, and the straight FFAG cell in blue. Two collimators are installed before the straight cell to set the Courant-Snyder parameters. The emittance measurement system is added after the straight cell to determine the exit parameters of the beam.

Since each energy has a different reference trajectory, the cell must be able to move horizontally to match the different trajectories without changing the magnetic field. Bellows before and after the cell allows the vacuum chamber to move along with the magnets without breaking the vacuum.

3.1.2 Incident beam

The linac can deliver 7 MeV and 11 MeV kinetic energy H^- particles. The horizontal phase advance measurements of these two different energies confirm or infirm the theory.

Collimator system design

Two collimators are installed in the beam line to set the emittance and the Courant-Snyder parameters. The size of the collimators and the distance between them indeed determine the Courant-Snyder parameters and the emittance. The emittance ϵ is a function of the collimator size a and the

distance between the two collimators b by

$$\epsilon_{100\%} = \frac{a}{2} \cdot \frac{a}{b} = \frac{a^2}{2b}. \tag{3.1}$$

A schematic view of the collimator system is presented in Fig. 3.3. If we backtrack the beam at the center of the collimator system, we have the particular property

$$\begin{aligned} \alpha &= 0, \\ \beta &= \frac{\left(\frac{a}{2}\right)^2}{\epsilon_{100\%}}. \end{aligned} \tag{3.2}$$

Size of the collimators has however to be small compared with the incident beam size. The collimator size is then 2 mm and the distance between the two collimators is set to 1530 mm. The distribution of the beam sets the rms emittance to 9σ of the total emittance. We then have at the entrance of the system

$$\begin{aligned} &\epsilon_{100\%} = 1.3\ \pi \text{ mm.mrad}, \\ &\epsilon_{rms} = \frac{\epsilon_{100\%}}{9} = 0.14\ \pi \text{ mm.mrad}, \\ &\beta = 0.77 \text{ m}, \\ &\alpha = 0. \end{aligned} \tag{3.3}$$

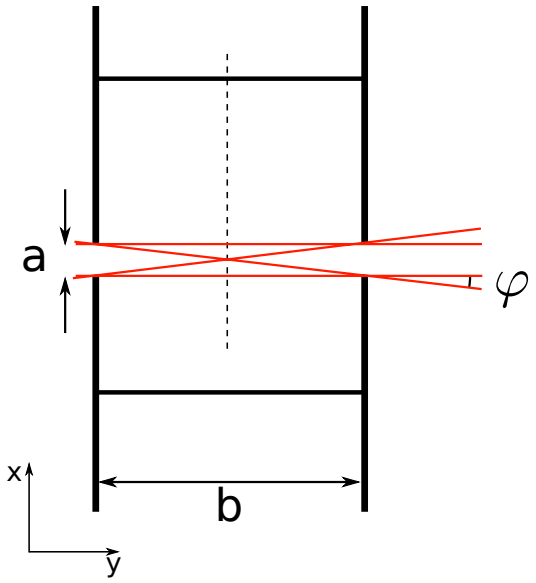

Figure 3.3: Schematic view of the collimator system.

To keep the collimators perpendicular to the beam, they are used as copper gaskets between two vacuum chambers. A picture of one collimator is presented on Fig. 3.4. Holes at the periphery have been made so that vacuum quality is not affected by the collimators.

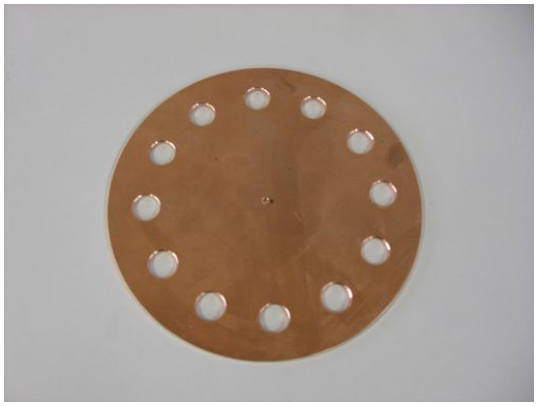

Figure 3.4: Picture of one of the collimator.

Alignment system of the collimators

Bellows has been installed upstream the first collimator to allow alignment of the vacuum chamber. Supports of the vacuum chamber have been equipped with alignment systems, shown in fig. 3.5. The precise alignment of the upstream collimator is done with a digital theodolite through the downstream collimator.

3.1.3 Courant Snyder parameters measurement system

The Courant Snyder parameters measurement system used in this experiment is similar to the emittance measurement "slit-grid method" [45], but with the grid replaced by a fluorescent screen. A schematic view of the system is presented in Fig. 3.6. The slit is used to measure the horizontal angle of the beam, and the slope of the line x' vs. x. When the slit is removed, the size of the beam on the screen fitted with a gaussian gives access to the rms beta value, and the center of the gaussian is taken as the position of the beam. Since the width of the slit is crucial for the accuracy of the measurement, a slit of 0.1 mm width has been manufactured and used in

Figure 3.5: Picture of one of the support with alignment system for the collimators.

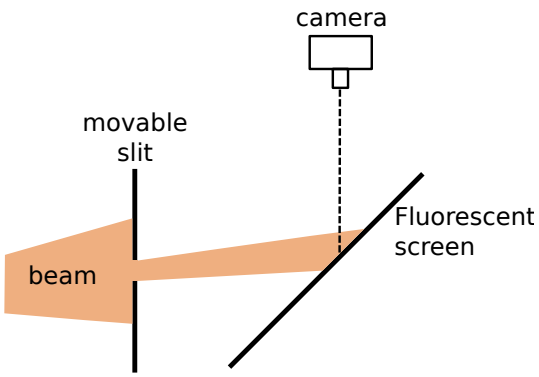

Figure 3.6: scheme of the Courant Snyder parameters measurement system installed after the Straight Cell.

the system. Since the beam is collimated and the slit is very narrow, the luminosity at the screen is small. A very sensitive fluorescent screen is then used in this experiment, the PI-200 screen from Mitsubishi Chemical.

3.1.4 Straight scaling FFAG magnet design

The prototype for the straight scaling FFAG cell is a FDF triplet.

Since the straight cell must be moved to match the different reference trajectories, one must limit the maximum necessary displacement. To that end, one would prefer to have a small dispersion, and m-value of the cell has been chosen to be 11 m^{-1}. The displacement between 11 MeV reference trajectory and 7 MeV reference trajectory is then around 2 cm. The parameters of the cell are summarized in Table 3.1.

Type	FDF
m-value	11 m^{-1}
Total length	4.68 m
Length of F magnet	15 cm
Length of D magnet	30 cm
Max. B Field (D magnet)	0.3 T
Max. B Field (F magnet)	0.2 T
Horizontal phase advance	87.7 deg.
Vertical phase advance	106.2 deg.

Table 3.1: Parameters of the Straight Cell.

Particle tracking in field model is done with the code developed at Kyoto University and described in App.B. Reference trajectories of 11 MeV and 7 MeV H^- particles are shown in Fig. 3.7, and their corresponding vertical magnetic field in Fig. 3.8. The computed beta-functions are shown in Fig. 3.9. The phase advances are constant and their values are 87.7 deg in horizontal and 106.2 deg in vertical, as it is shown in Fig. 3.10.

Pole shape design

A "C" type magnet has been chosen to have an easier access to the pole for field measurement. The pole shape has been designed first in 2 dimensions with the finite element computation software POISSON[46]. The final field configuration is presented in Fig. 3.11. The minimum full gap size has been chosen to be 2.3 cm, to limit the ampere turns. Field clamps with a 12 mm thickness have been adjusted at 60 mm from the poles to match the fringe

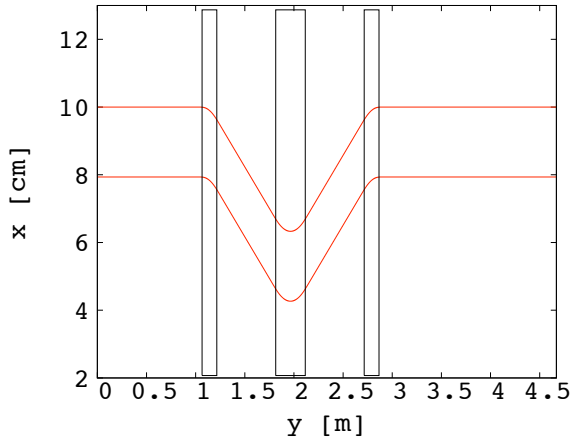

Figure 3.7: 11 MeV and 7 MeV reference trajectories in the Straight FFAG line with field model.

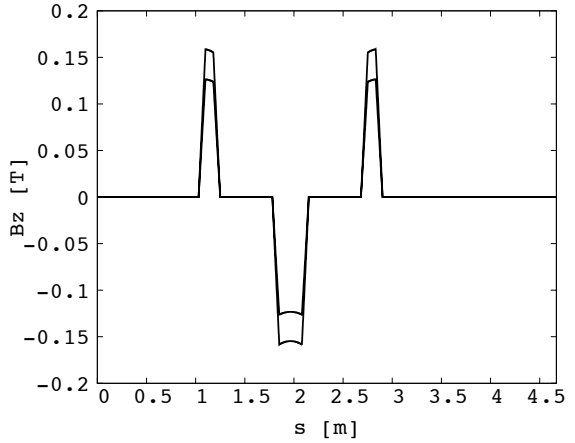

Figure 3.8: Vertical magnetic field for 11 MeV and 7 MeV reference trajectories in the Straight FFAG line with field model.

field of the field model. The pole shape has then been optimized in 3 dimensions with TOSCA code (see Fig. 3.12 and 3.13). Tracking step by step using Runge Kutta integration has been done in field maps from TOSCA. The interpolation of the field between the map nodes is done linearly in 3 dimensions. The reference trajectories of 7 MeV and 11 MeV are shown in Fig. 3.14, and their corresponding vertical magnetic field in Fig. 3.15. The beta-functions in the system are shown Fig. 3.16. The local phase advances in the Straight Cell are plotted in Fig. 3.17. The results show a constant horizontal phase advance, since the local m-value in the field map is constant

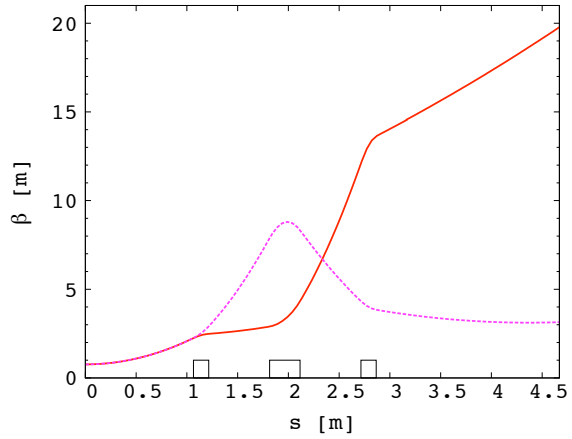

Figure 3.9: Horizontal (plain red) and vertical (dotted purple) beta-functions in the Straight FFAG line with field model.

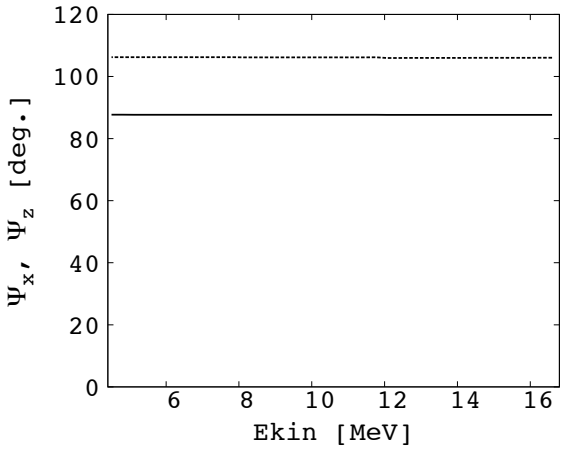

Figure 3.10: Horizontal (plain) and vertical (dotted) local phase advances versus kinetic energy in the Straight FFAG line.

(see Fig. 3.18) and a slightly changing vertical phase advance, typical of the scaling FFAGs, because the fringe fields do not scale due to the pole shape. It would be possible to adjust the length of the fringe field by adjusting the effective field boundaries [47], but rectangular magnets have been kept for economical reasons.

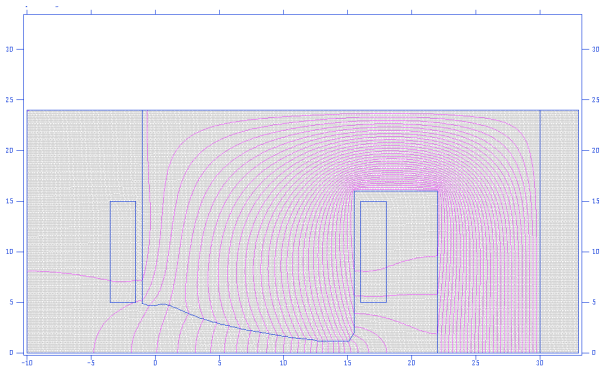

Figure 3.11: Pole shape from POISSON.

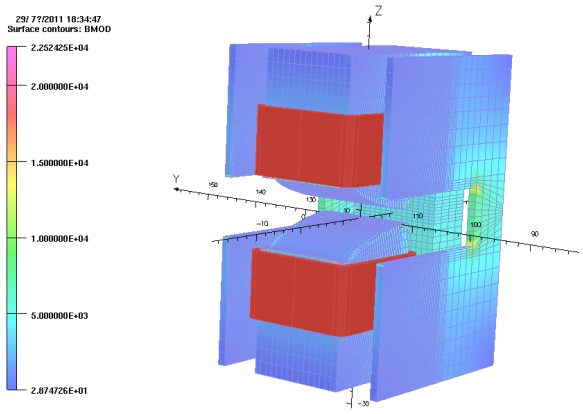

Figure 3.12: Magnetic field in F magnet (TOSCA model).

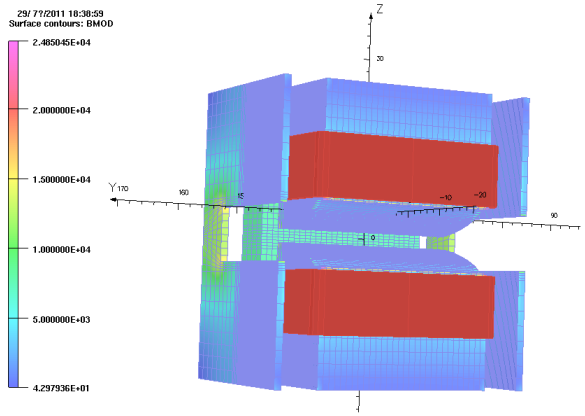

Figure 3.13: Magnetic field in D magnet (TOSCA model).

Coil design

A first estimation of the ampere turns can be calculated with

$$NI = \frac{d}{\mu_0} B, \tag{3.4}$$

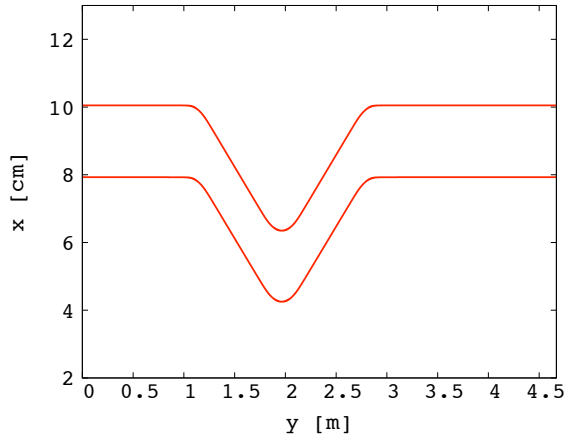

Figure 3.14: 11 MeV and 7 MeV reference trajectories in the Straight FFAG line with TOSCA field maps.

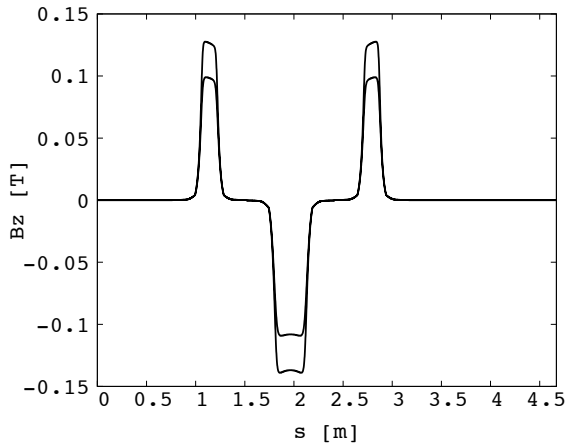

Figure 3.15: Vertical magnetic field for 11 MeV and 7 MeV reference trajectories in the Straight FFAG line with TOSCA field maps.

with d the gap size, μ_0 the vacuum permeability and B the magnetic field. A numerical application of Eq. 3.4 with the minimum gap size gives 1830 AT per coil in the F magnet and 2750 AT per coil in the D magnet. After optimization by computation with TOSCA, the ampere turns is finally 1950 AT per coil in the F magnets, and 3200 AT per coil in the D magnet. On the one hand, use of air cooling coils would be possible, but the needed amount of copper would be expensive. On the other hand, hollow conductors are even more expensive. The chosen solution is then indirect water cooling. It is composed of plain copper wires with water-cooled plates fixed on them.

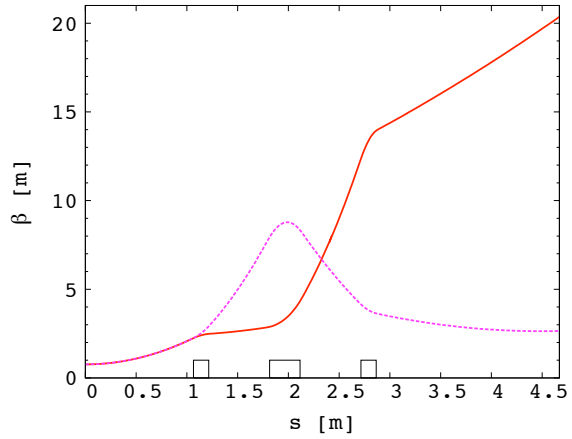

Figure 3.16: Horizontal (plain red) and vertical (dotted purple) beta-functions in the Straight FFAG line with Tosca field maps.

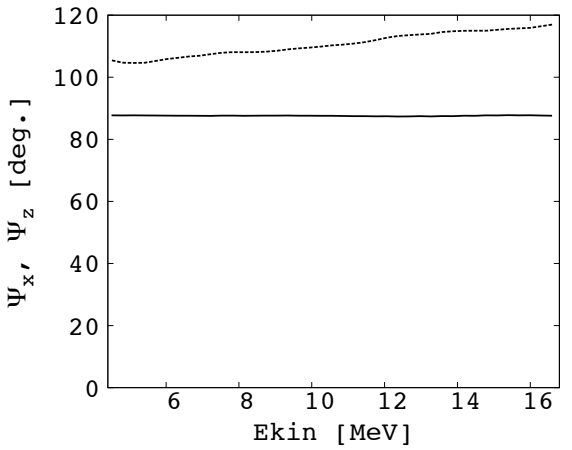

Figure 3.17: Horizontal (plain) and vertical (dotted) local phase advances versus kinetic energy in the Straight FFAG line.

Epoxy is used for insulating the wires from each other with a good thermal conductivity. The wire is chosen with a rectangular section with 2 mm×5 mm dimensions. 72 turns per coil are distributed in 18 turns with 4 layers. The current density is then 2.7 A/mm^2 in the F magnet, and 4.4 A/mm^2 in the D magnet. The total power consumption of the three magnets is around 1 kW. The water cooling system is powered with the chiller EYELA CA 1112, with a cooling capacity of 1200 W.

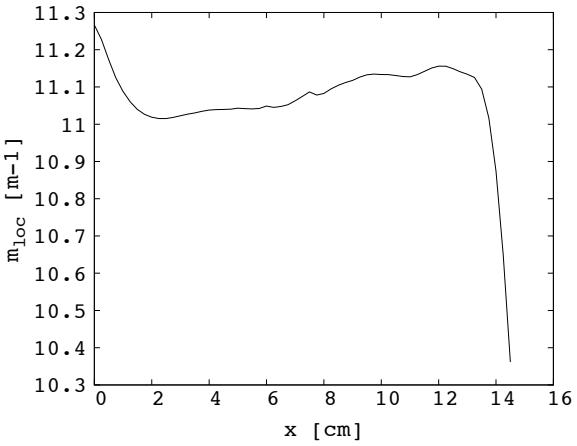

Figure 3.18: Local m value versus horizontal abscissa in the Straight FFAG line. The good field region is kept between 2 cm and 13 cm.

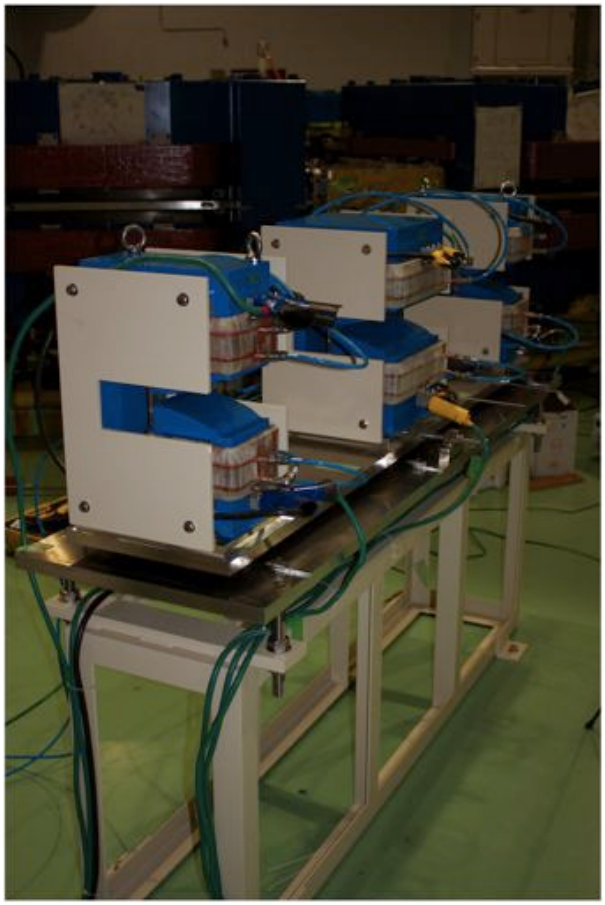

Figure 3.19: Picture of the straight scaling FFAG magnets prototype.

Power supply

A power supply has been dedicated to each magnet. Each power supply range is 100 A maximum for a maximum voltage of 30 V. According to TOSCA, one F magnet uses 27 A for 5.4 V (100 mΩ per coil), and the D magnet needs 44 A for 12.3 V (140 mΩ per coil).

Moving system

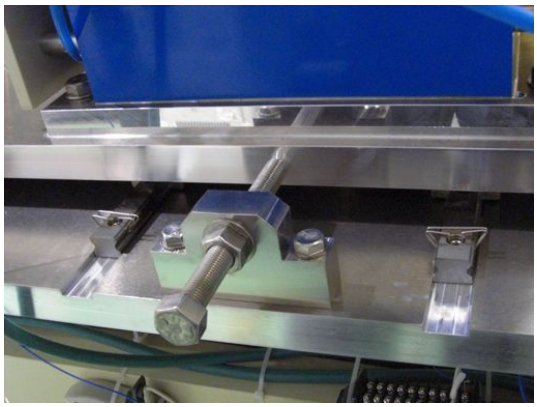

Figure 3.20: Picture of the moving system of the magnets.

It is a ball-bearing system that makes the sliding of the magnets possible. A picture of the system is presented in Fig. 3.20. A ruler is fixed at the table to measure the displacement.

Vacuum chamber

The minimum gap size is 2.3 cm. To have a larger aperture in the chamber, the vacuum chamber in the magnets follows the pole shape, as it is shown in Fig. 3.21.

3.1.5 Control system

A control system based on EPICS is used to drive the power supplies. To protect the coils from burning, an interlock system has also been made. A data logger measures the temperature of the upper coil of the D magnet. If the measured temperature is higher than 90 deg Celsius, the three power supplies are then set to 0 A.

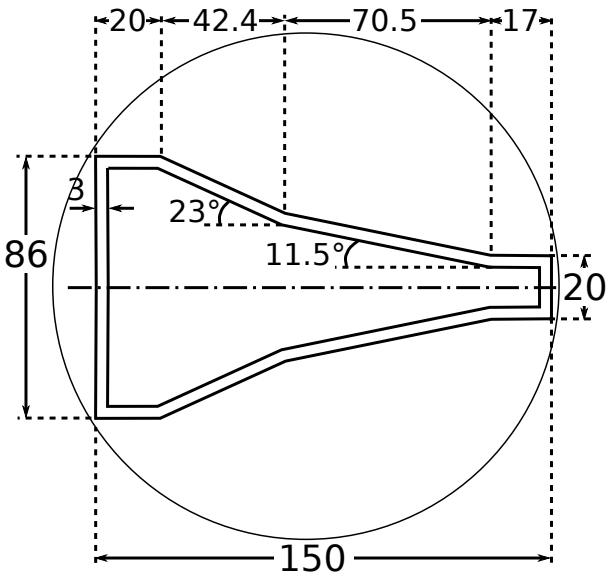

Figure 3.21: Vacuum beam duct in the magnet.

3.2 Field measurement experiment

The magnets have been manufactured and delivered. To check the manufacturing precision and have tracking in measured field maps, measurement of the field has been done.

3.2.1 Field map creation

A layout of the field measurement experiment is presented in Fig. 3.22. A

Figure 3.22: Picture of the field measurement layout.

3-dimensional magnetic probe is attached to a moving robot, controlled by the system YAMAHA RCX 142 series. The three magnets are first aligned with a theodolite, then the probe robot is aligned according to the magnet system. Since the available range of the robot is too small for the whole cell, each magnet is measured separately, and the probe robot is moved and realigned for each magnet.

To calibrate the different power supplies, the probe is installed at the center of the measured magnet, and the current value is set so that the corresponding vertical magnetic field matches with the TOSCA model. Thus the power supply for the first F magnet "F_1" is set to 28.67 A, for the D magnet "D_2" 48.34 A, and for the second F magnet "F_3" 29.10 A.

The field is measured on 3 vertical layers: in the mid-plane ($z = 0$), $z = +5$ mm and $z = -5$ mm. Each plane is measured in the good field region, with a horizontal step size of 5 mm, and a longitudinal step size of 10 mm. A margin of 20 cm from both sides of each magnet is added to the effective field boundaries to measure the fringe fields. The resulting field maps for the vertical component in the mid-plane for the magnets F_1, D_2 and F_3 are shown in Fig. 3.23, Fig. 3.24 and Fig. 3.25, respectively.

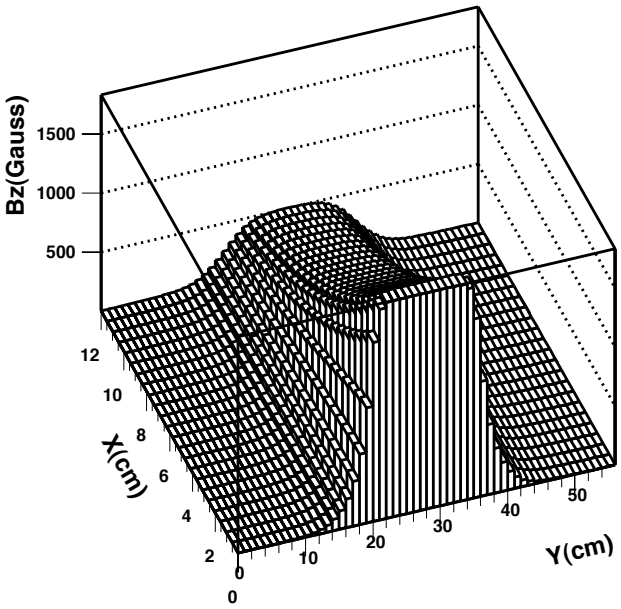

Figure 3.23: Field map of the magnet F_1 in the mid-plane.

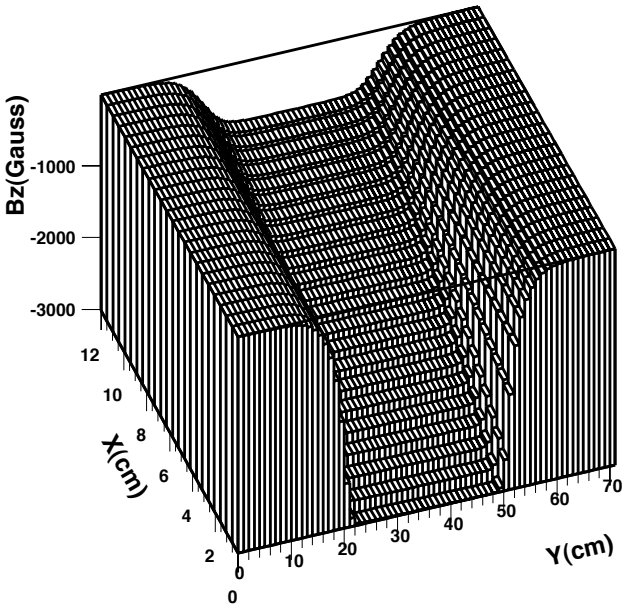

Figure 3.24: Field map of the magnet D_2 in the mid-plane.

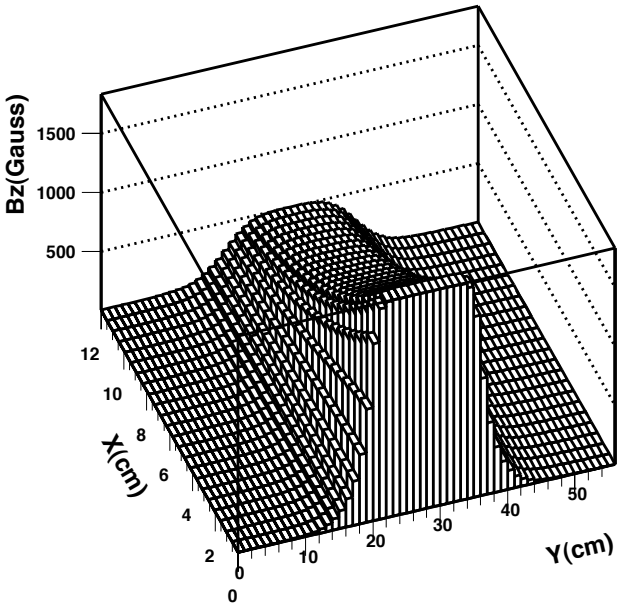

Figure 3.25: Field map of the magnet F_3 in the mid-plane.

Comparisons with TOSCA field maps are presented in Fig. 3.26, Fig. 3.27 and Fig. 3.28 for the magnets F_1, D_2 and F_3, respectively. The agreement is

good, with a difference mainly in the fringe fields areas, less than 1% of the field for the different magnets.

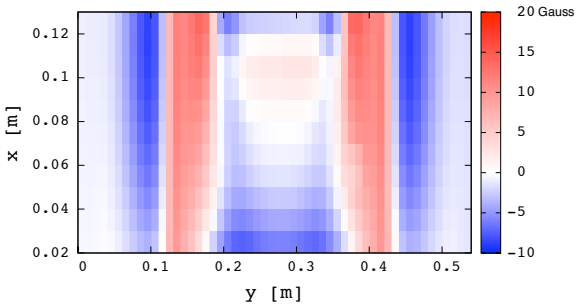

Figure 3.26: Difference of the vertical magnetic field in the mid-plane in Gauss between the TOSCA field map and measured field map of the magnet F_1.

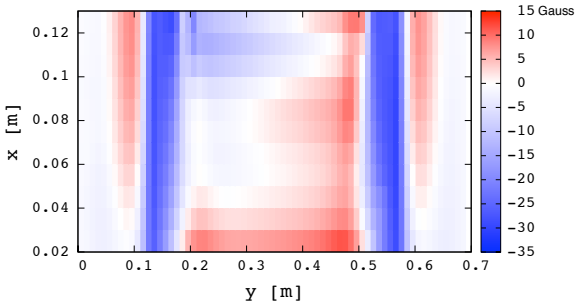

Figure 3.27: Difference of the vertical magnetic field in the mid-plane in Gauss between the TOSCA field map and measured field map of the magnet D_2. A small effect of skew misalignment of the probe can be seen in this figure.

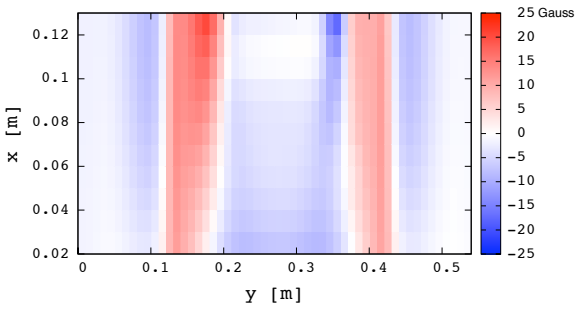

Figure 3.28: Difference of the vertical magnetic field in the mid-plane in Gauss between the TOSCA field map and measured field map of the magnet F_3.

3.2.2 Stability of magnetic field

The probe is installed at the center of the magnet F_3. After waiting for 30 minutes for stabilization of the magnetic field, Data is taken every 20 seconds during 8 hours. At this point the average value is 841 G. The results are presented in Fig. 3.29. They are consistent with long-term Eddy currents stabilization, typical in static magnets.

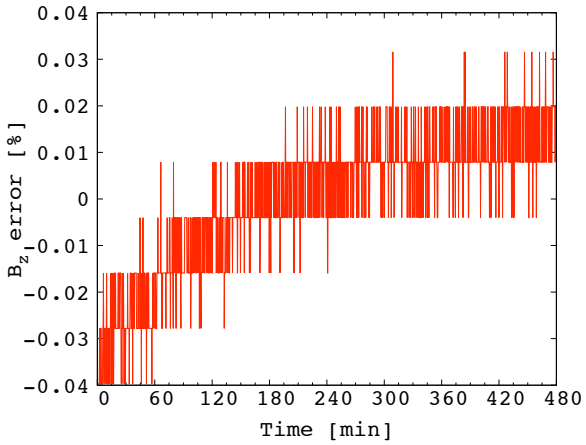

Figure 3.29: fluctuation of the field measurement layout.

3.2.3 Experimental results analysis

Particle tracking with Runge-Kutta integration has been done in the measured field map. Reference trajectories of 11 MeV and 7 MeV H^- particles are shown in Fig. 3.30, and their corresponding vertical magnetic field in Fig. 3.31. The computed beta-functions are shown in Fig. 3.32.

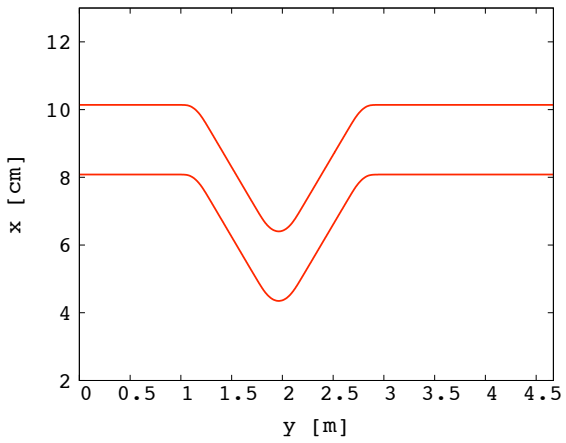

Figure 3.30: 11 MeV and 7 MeV reference trajectories in the Straight FFAG line with measured field maps.

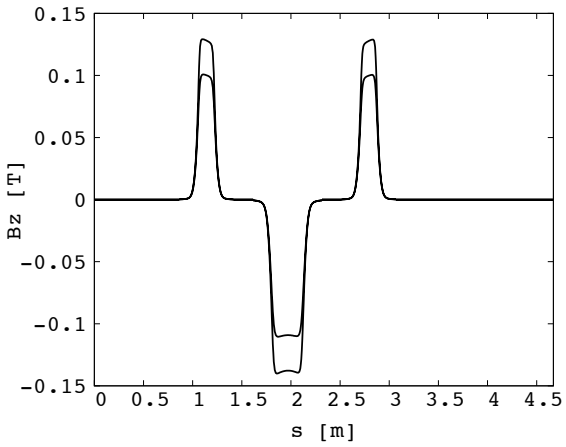

Figure 3.31: Vertical magnetic field for 11 MeV and 7 MeV reference trajectories in the Straight FFAG line with measured field maps.

The comparison of the local m-value and the phase advances in horizontal and vertical in measured field map and in TOSCA field maps are shown in

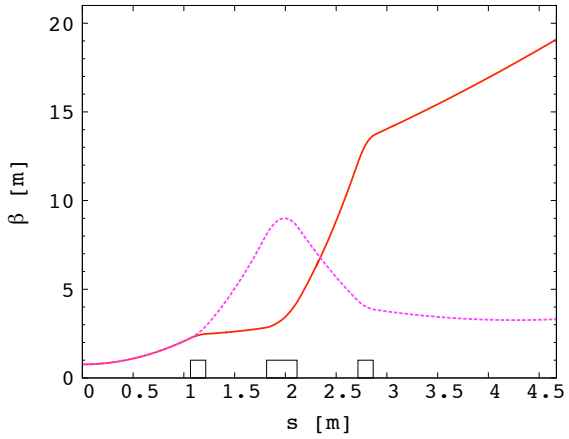

Figure 3.32: Horizontal (plain red) and vertical (dotted purple) beta-functions in the Straight FFAG line with measured field maps.

Fig. 3.33 and in Fig. 3.34, respectively. The agreement is within 1% for the m-value and for the horizontal phase advances, which is in the acceptable range. The horizontal phase advance measurement is indeed an indirect method, and a precision better than 1% is difficult to achieve. The agreement is within 5% for the vertical phase advances, due to the difference in the fringe fields, which is also in the acceptable range. It validates the manufacturing of the magnets. Since the precision of the TOSCA field maps is better than in the measured field maps (more nodes in the maps, no measure alignment error), the comparison of the measured phase advances is done with TOSCA tracking results.

3.3 Horizontal phase advance measurement experiment

The goal of this experiment is to measure the phase advance for 7 MeV and 11 MeV in the straight scaling FFAG cell prototype. To achieve this, the Courant-Snyder parameters as well as position and angle of the beam is measured at the exit of the Straight Cell when it is launched off its reference trajectory. The linear transfer matrix of the line is

$$\begin{pmatrix} x_1 \\ x_1' \end{pmatrix} = \begin{pmatrix} \sqrt{\frac{\beta_1}{\beta_0}}\left(\cos\psi + \alpha_0 \sin\psi\right) & a_{12} \\ \frac{(\alpha_0-\alpha_1)\cos\psi - (1+\alpha_0\alpha_1)\sin\psi}{\sqrt{\beta_1\beta_0}} & a_{22} \end{pmatrix} \cdot \begin{pmatrix} x_0 \\ 0 \end{pmatrix},$$

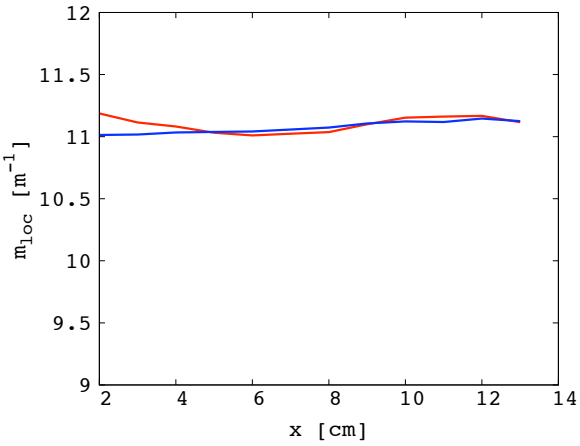

Figure 3.33: Comparison of local m-value in TOSCA map (blue) and in measured map (red) in the good field region.

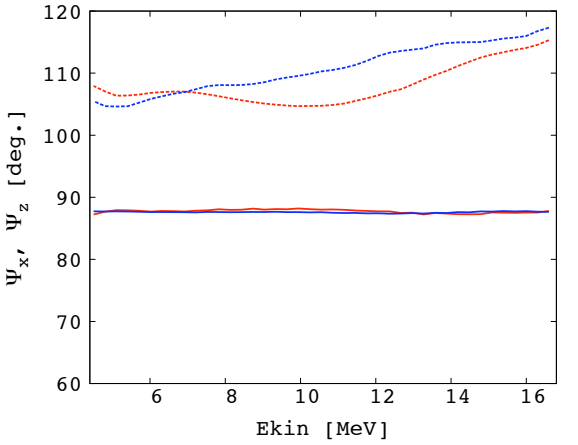

Figure 3.34: Comparison of local horizontal (plain) and vertical (dotted) phase advances in TOSCA map (blue) and in measured map (red) in the good field region.

with x_1 and x_1' the distance and the angle to the reference trajectory at the exit of the cell, respectively. x_0 is the distance to the reference trajectory at the entrance of the cell. No angle with the reference trajectory is added at the entrance of the cell. α_0 and β_0 are the Courant-Snyder parameters at the entrance of the cell, while α_1 and β_1 are the Courant-Snyder parameters at the exit of the cell. ψ is the linear phase advance. The system of equations

to be solved is then

$$\begin{cases} \sqrt{\frac{\beta_1}{\beta_0}}\left(\cos\psi + \alpha_0 \sin\psi\right) = \frac{x_1}{x_0} \\ \frac{(\alpha_0-\alpha_1)\cos\psi - (1+\alpha_0\alpha_1)\sin\psi}{\sqrt{\beta_1\beta_0}} = \frac{x_1'}{x_0} \end{cases}, \tag{3.5}$$

and we get

$$\begin{cases} \sin\psi = \sqrt{\frac{\beta_0}{\beta_1}}\frac{1}{x_0(1+\alpha_0^2)}\left((\alpha_0-\alpha_1)x_1 - \beta_1 x_1'\right) \\ \cos\psi = \sqrt{\frac{\beta_0}{\beta_1}}\frac{1}{x_0(1+\alpha_0^2)}\left((1+\alpha_0\alpha_1)x_1 + \alpha_0\beta_1 x_1'\right) \end{cases}. \tag{3.6}$$

So we can calculate the linear phase advance ψ by:

$$\tan\psi = \frac{(\alpha_0-\alpha_1)x_1 - \beta_1 x_1'}{(1+\alpha_0\alpha_1)x_1 + \alpha_0\beta_1 x_1'}. \tag{3.7}$$

Since $\alpha_0 = 0$, Eq. 3.7 simplifies as

$$\tan\psi = -\alpha_1 - \frac{\beta_1 x_1'}{x_1}. \tag{3.8}$$

3.3.1 Courant-Snyder parameters, position and angle measurement

The experiment consists of 6 series of data, taken at a different magnet position. The first position magnet corresponds to the reference trajectory

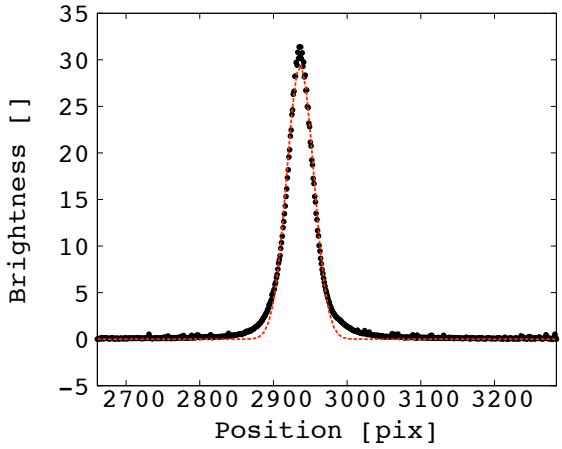

Figure 3.35: Gaussian fit (dotted red) of the H^0 brightness for 11 MeV reference trajectory. The reference point in this case is 2936 pixel.

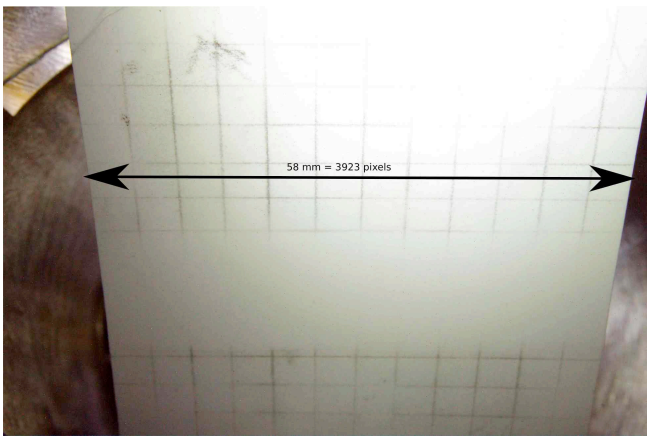

Figure 3.36: Example of a reference picture for conversion of distance from pixel into millimeters. This particular picture is the case of 11 MeV reference trajectory.

position (position 92 mm for 11 MeV, position 75 mm for 7 MeV), from which the Courant Snyder parameters are extracted. Then the position +10 mm (position 102 mm for 11 MeV, position 85 mm for 7 MeV) and the position -10 mm (position 82 mm for 11 MeV, position 65 mm for 7 MeV) gives the angle and position of the beam off the reference trajectory. The second order is canceled by adding the 2 results. To have more statistical data, Courant Snyder parameters are extracted from all magnet positions. Data consist of pictures of the fluorescent screen with different slit positions.

The alignment of the screen with the collimators is done with H^0 particles, assuming that these particles are homogeneously distributed at the collimator system. The picture of the screen with the slit at the central position (aligned with the theodolite) is used to determine the reference point of the picture. A gaussian fit of the brightness in the H^0 patch region gives indeed the alignment of the screen with the collimators. Such a fit is presented for the 11 MeV reference trajectory in Fig. 3.35. Since a H^0 beam is present at the screen, the collimator system is installed off the mid-plane to separate the two beams at the screen, using the vertical betatron oscillation.

The position of the screen is given in pixels, and can be converted into millimeters with a reference picture by a ratio r (see Fig. 3.36). From the position at the screen and the position of the slit, we can get the angle of the

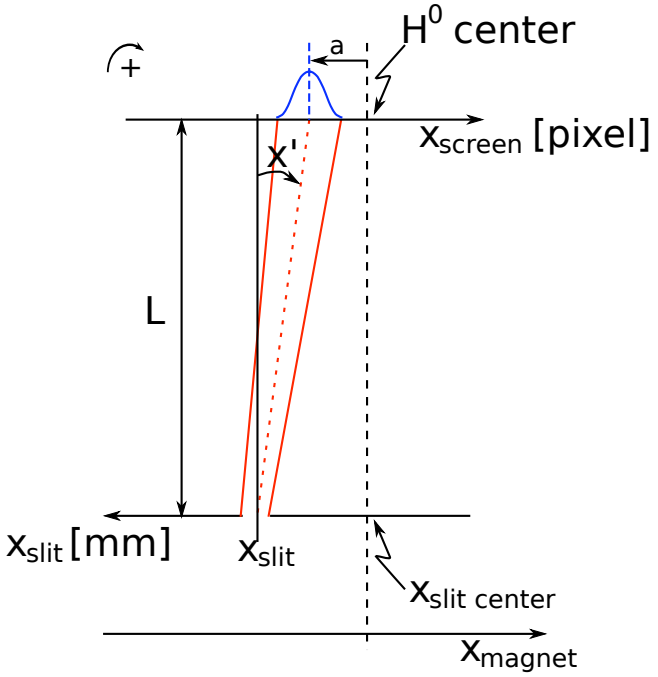

Figure 3.37: Definition of the angle measurement.

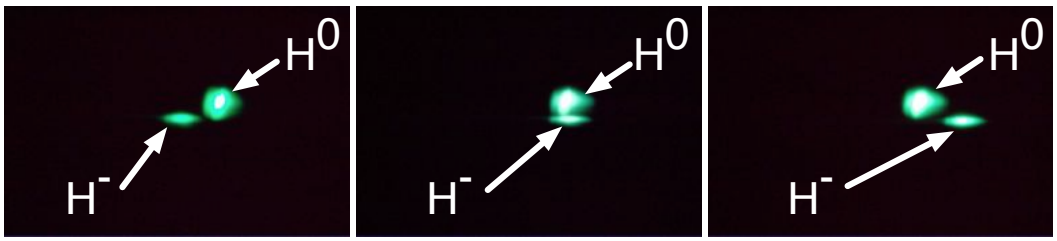

Figure 3.38: Pictures of the fluorescent screen without slit for the 11 MeV case. The top patch comes from the H^0 beam, and the lower one comes from the H^- beam. The left picture represents the -10 mm displacement off the reference trajectory, the middle one the reference trajectory, and the right one the +10 mm displacement off the reference trajectory.

beam x' with the parameters defined in Fig. 3.37

$$x' = \arctan \frac{a \cdot r + (x_{slit} - x_{slit\ center})}{L}. \tag{3.9}$$

The slope *slope* of the line $x' = slope \cdot x_{slit} + b$ gives the ratio α_2/β_2 at the slit. The pictures without slit, as it is shown in Fig. 3.38 for the 11 MeV case, fitted by a gaussian can give the rms beam size at the screen. Assuming

	x_1 (mm)	x_1' (mrad)	σ (mm)	$\frac{\alpha_2}{\beta_2}$ (m^{-1})
Ref. traj. 11 MeV (pos. 92 mm)	0.1	-0.5	1.7	-0.09
+10 mm 11 MeV (pos. 102 mm)	1.4	-1.8	1.6	-0.08
-10 mm 11 MeV (pos. 82 mm)	-2.6	2.9	1.4	-0.11
Ref. traj. 7 MeV (pos. 75 mm)	0.6	0.5	1.1	-0.09
+10 mm 7 MeV (pos. 85 mm)	0.3	-1.9	1.1	-0.05
-10 mm 7 MeV (pos. 65 mm)	-3.4	2.2	1.8	-0.11

Table 3.2: Results of the position (x_1), angle (x_1'), rms beam size at the screen (σ) and ratio $\frac{\alpha_2}{\beta_2}$ at the slit in the Straight Scaling FFAG experiment.

the geometrical emittance from the collimator system, we can get the beta function at the screen by

$$\beta_1 = \frac{\sigma^2_{rms\ screen}}{\epsilon_{rms}}. \tag{3.10}$$

By tracking in the drift space between the slit and the screen, we can get the alpha parameter at the screen by

$$\alpha_1 = \beta_2 \left(\frac{\alpha_2}{\beta_2}\right) - L\left(\frac{1}{\beta_2} + \beta_2 \left(\frac{\alpha_2}{\beta_2}\right)^2\right), \tag{3.11}$$

with the beta function β_2 at the slit given by

$$\beta_2 = \frac{\beta_1 + \sqrt{\beta_1^2 - 4L^2\left(1 - 2L\left(\frac{\alpha_2}{\beta_2}\right) + L^2\left(\frac{\alpha_2}{\beta_2}\right)^2\right)}}{2\left(1 - 2L\left(\frac{\alpha_2}{\beta_2}\right) + L^2\left(\frac{\alpha_2}{\beta_2}\right)^2\right)}. \tag{3.12}$$

The measured parameters are summarized in Table 3.2.

3.3.2 Experimental results analysis

From these results and Eq. 3.8, we obtain that phase advance

$$\boxed{\psi_{11\ MeV} = 87.5\ deg,}$$

for 11 MeV, and

$$\boxed{\psi_{7\ MeV} = 86.1\ deg,}$$

for 7 MeV. We then have a difference of 1.6% between the two energies, which is in the acceptable range. There is no difference of phase advance

	$\bar{x_1}$ (mm)	$\bar{x_1'}$ (mrad)	$\bar{\beta_1}$ (m)	$\bar{\alpha_1}$	$\psi_{exp.}$ (deg)	$\psi_{track.}$ (deg)
11 MeV	**2.0**	**-2.4**	**17.7**	**-1.5**	**87.5** $\pm$ 3.3	**87.5**
7 MeV	**1.8**	**-2.1**	**11.7**	**-1.0**	**86.1** $\pm$ 9.6	**87.6**

Table 3.3: Results of the position ($\bar{x_1}$) and angle ($\bar{x_1'}$), Courant Snyder parameters ($\bar{\beta_1}$ and $\bar{\alpha_1}$) and resulting phase advance ($\psi_{exp.}$) in the Straight Scaling FFAG experiment. Tracking phase advance $\psi_{track.}$ in TOSCA field maps is also presented for comparison.

with tracking in the 11 MeV case, and it is 1.7% for the 7 MeV case. This good agreement clarifies the straight scaling law. The results are summarized in Table 3.3.

The errors, presented in Table 3.3, are dominated by the beta function error, due to the fluctuation of the beam size. It is acceptable for 11 MeV (3.7%), but is quite large for 7 MeV (11.1%), because the incident beam fluctuates, degrading the emittance quality. It affects the beam size at the screen, with an error three times bigger than in the 11 MeV case. Since the cause of the error is from the incident beam, it is inevitable to have a large error for 7 MeV.

Chapter 4

Applications

The straight scaling law has thus been confirmed through experiment. This new law and combinations with circular scaling FFAG cells open a wide range of applications, described in this chapter. Small excursion insertions are first developed, then zero-chromatic racetrack FFAG rings are shown. Modular systems in zero-chromatic FFAGs with long drift sections for injection and extraction are also presented. Dedicated insertions are then described, with the example of a low-vertical beta function insertion. Finally gantries for hadrontherapies are briefly introduced.

Designs in this section have been developed with the code developed at Kyoto University Research Reactor Institute and described in App. B.

4.1 Small excursion insertions for rf cavities

4.1.1 Neutrino factory with harmonic number jump acceleration

	Ring main part	Reduced excursion area	First dispersion suppressor	Second dispersion suppressor
Cell type	DFDF	DFDF	DFDF	DFDF
Cell opening angle [deg.]	5.	2.25	4.5	3.5
Mean radius [m]	136.2	332.3	155.5	184.9
Field index k	130	638	169.9	283.5
Horiz. phase adv./cell [deg.]	87.4	86.4	90.0	90.0
Vert. phase adv./cell [deg.]	50.6	32.0	44.4	34.6
Number of these cells /ring	8×4	8×4	4×4	4×4

Table 4.1: Parameters of the HNJ muon ring.

The idea of a facility producing neutrinos from muon beams, so-called a neutrino factory, is widely prospected these days [11]. The interest of this facility is that the intense generated neutrino flux and mixture is well-controlled and suitable for physics experiments beyond the standard model. In this scheme, rapid acceleration is essential to limit the number of muons lost by decay. The baseline is based on linear accelerators, recycling linear accelerators (RLAs) and FFAG for the last stage [48], as it is shown in Fig. 4.1.

However, FFAGs are more cost-effective than RLAs, since a different arc is needed for each path in the linear accelerator. The so-called harmonic number jump (HNJ) acceleration allows the acceleration with constant rf frequencies compatible with the present baseline scheme in zero-chromatic FFAGs [49, 50].

The condition of synchronization between the revolution frequency f_{rev} of a particle and the frequency of oscillation of the rf field f_{rf} can be written

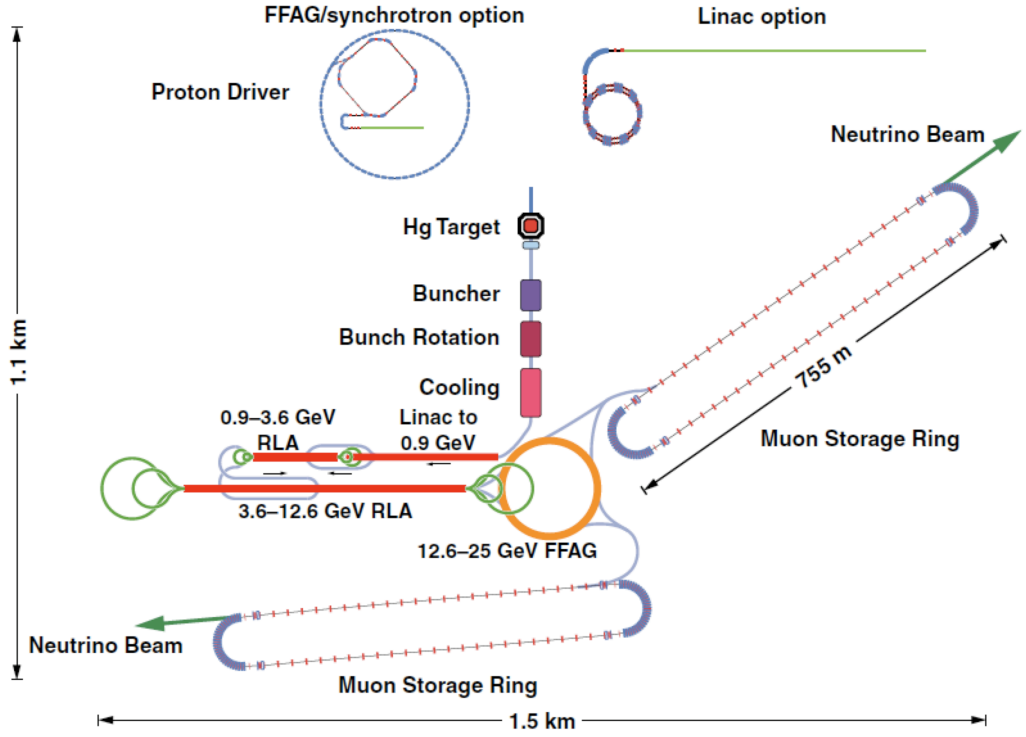

Figure 4.1: Schematic view of the neutrino factory baseline design, from the IDS-NF [48].

as

$$f_{rf} = h \cdot f_{rev}, \tag{4.1}$$

where h is an integer called the harmonic number. The principle of the HNJ acceleration is to maintain this condition in the ring by changing the harmonic number h of an integer number every turn. However, for relativistic particles, the required variation of time of flight only comes from the variation of path length between each turn. An acceleration over a number of turns N_t, with exactly one harmonic jump each turn, gives then an average excursion from injection to extraction [49]

$$\text{total average orbit excursion} = \frac{N_t}{2\pi} \cdot \lambda_{rf}. \tag{4.2}$$

The average excursion is thus larger than the diameter of a pillbox type rf cavity for a number of turns superior to 5, creating cavity design issues.

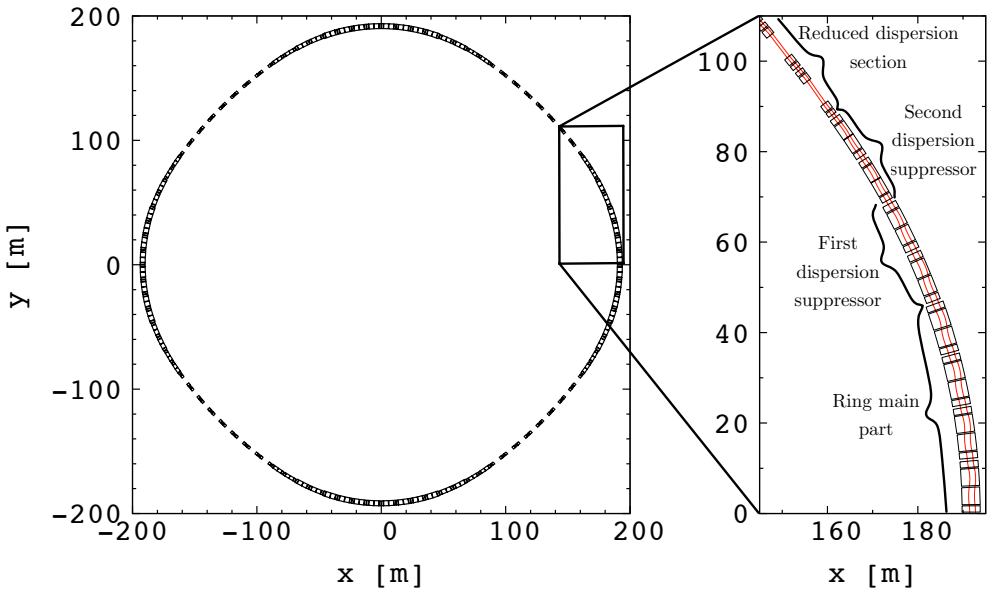

Figure 4.2: Schematic view with the position of the magnet effective field boundaries (left) of the HNJ muon ring. A zoom of the ring is detailed (right). The closed orbits corresponding to 3.6 and 12.6 GeV μ^+ are shown in red lines.

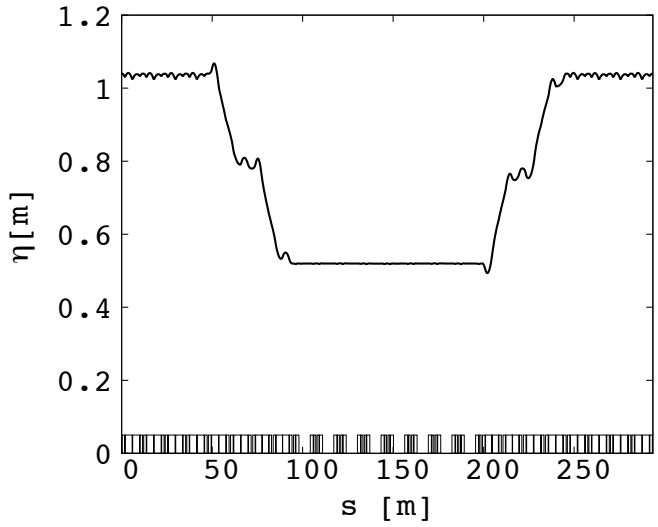

Figure 4.3: Dispersion function for μ^+ particles in a quarter of the HNJ muon ring at 5 GeV, centered on the low excursion area.

4.1.2 Reduced excursion insertions

To overcome this constraint, the excursion can vary along the ring, introducing reduced excursion insertions in which cavities could be installed, and large excursion sections where the necessary difference in path length could be achieved.

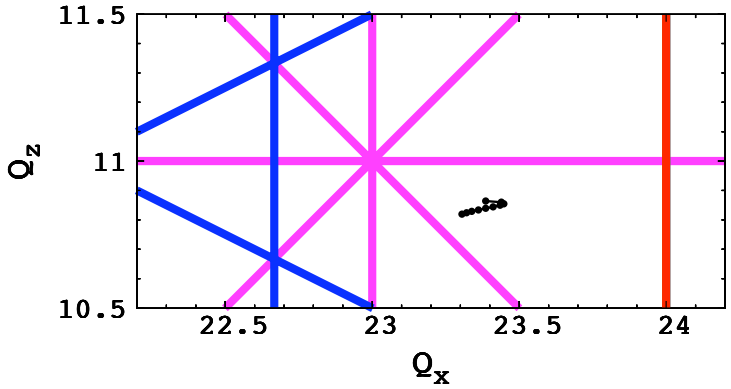

Figure 4.4: Variation of the betatron ring tunes for μ^+ particles in the HNJ muon ring, plotted every 1 GeV from 3.6 to 12.6 GeV in the tune diagram. Structural normal resonance lines up to octupole are superimposed.

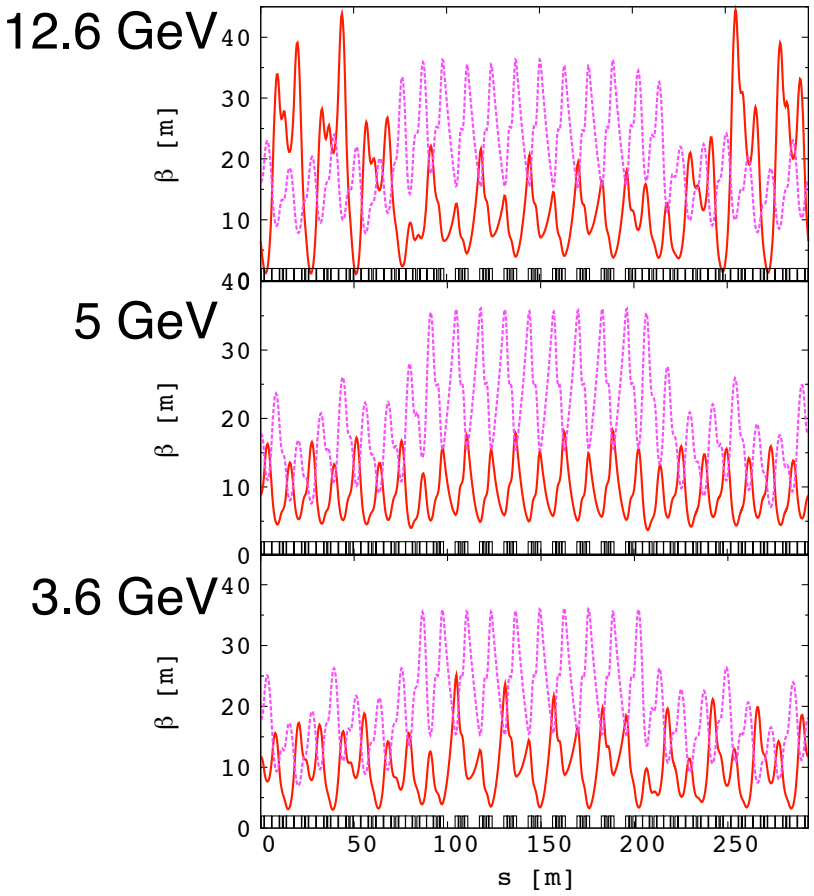

Figure 4.5: Horizontal (plain red) and vertical (dotted purple) periodic beta-functions for μ^+ particles of a quarter of the HNJ muon ring for 12.6 GeV (top scheme), 5 GeV (middle scheme), and 3.6 GeV (bottom scheme). The plot is centered on the low dispersion area.

An example of lattice for a 3.6 GeV to 12.6 GeV (kinetic energy) muon ring with this particular feature is designed, with its parameters given in Table 4.1. A schematic layout of this ring is shown in Fig. 4.2. The dispersion is divided by a factor of 2 in the area dedicated for cavities, as it is shown in Fig. 4.3. The beta-functions at 3.6 GeV, 5 GeV and 12.6 GeV are presented in Fig. 4.5. The tune variation is kept within 0.15 in horizontal and 0.1 in vertical, far from harmful resonances, as it is shown in the tune diagram in Fig. 4.4. Acceptance study at fixed energy (3.6 GeV and 12.6 GeV) has been done, and maximum stable amplitude over 100 turns are presented in

Fig. 4.6.

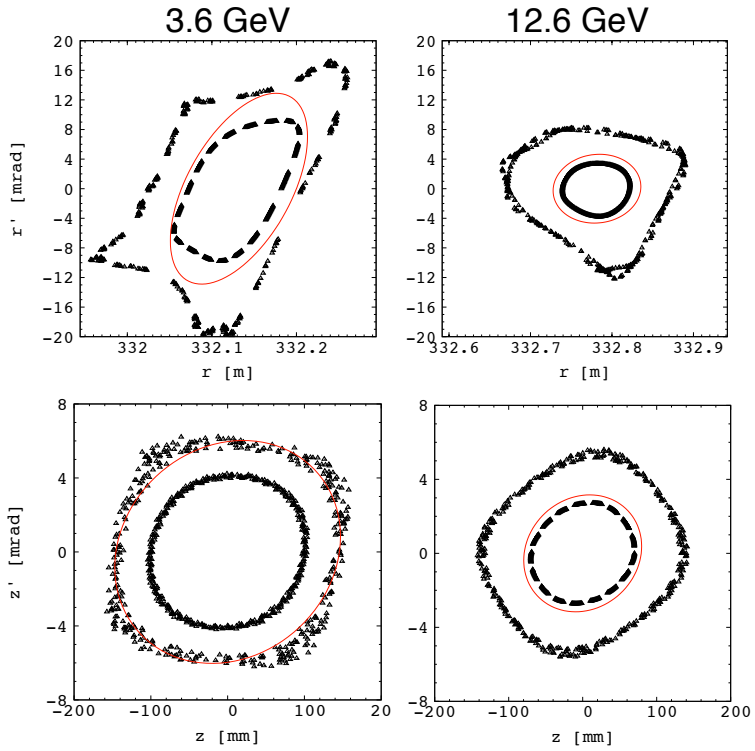

Figure 4.6: Horizontal (top) and vertical (bottom) Poincaré map showing the maximum amplitude for a stable motion over 100 turns at 3.6 GeV (left) and 12.6 GeV (right) μ^+ particles. The red ellipses represent the required transverse acceptance of this scheme (30, 000 π mm.mrad normalized).

4.2 FFAG race-track ring

4.2.1 Very low energy neutrino factory with a muon decay ring

The interest for Very Low Energy Neutrino Factory (VLENF) with a muon decay ring is also growing recently for neutrino physics experiment beyond the standard model [51, 52]. A race-track storage ring is then needed, and a lattice made of linear elements has been proposed. If the transverse acceptance at fixed energy is large, chromaticity of this ring limits the momentum

	Circular Section	**Straight Section**
Type	FDF	DFD
Cell radius [m]/opening angle [deg] or Length [m]	16/22.5	6
k-value or m-value	11	3.9 m^{-1}
Packing factor	0.9	0.1
Horizontal phase advance /cell [deg]	90.0	13.0
Vertical phase advance /cell [deg]	22.5	15.2
Average dispersion /cell [m]	1.4	0.3
Number of cells /ring	8×2	18×2

Table 4.2: Parameters of the VLENF racetrack lattice.

acceptance to about ±1% around the central momentum, which drastically limits the brightness at the detector. An advanced scaling FFAG race-track storage ring would then be a solution to increase this momentum acceptance. A preliminary study could sketch the possibilities of such a lattice. The

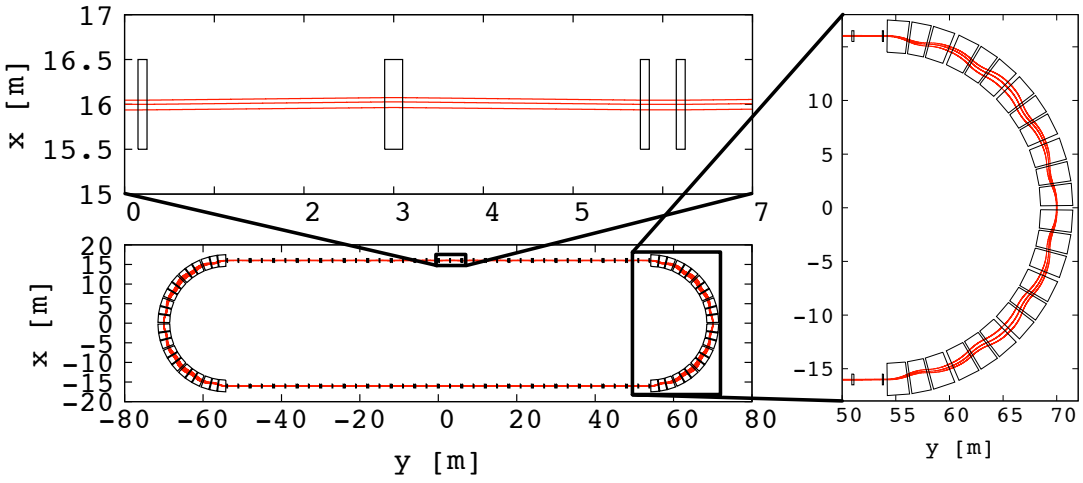

Figure 4.7: Top view of the racetrack FFAG lattice (bottom left scheme). The top left scheme shows a zoom on the straight section and the right scheme a zoom on the arc section. p_0, p_{min}, and p_{max} muon closed orbits are shown in red. Effective field boundaries with collimators are shown in black.

momentum range of tracked muon μ^+ for this lattice is chosen to be $\pm 16\%$ around the central momentum 2 GeV (kinetic energy). The parameters of the straight scaling FFAG cell and of the circular scaling FFAG cell are summarized in Table 4.2.

Closed orbits of p_0, p_{min}, and p_{max} particles are shown in a schematic layout of the lattice in Fig. 4.7. Dispersion at p_0 is shown in Fig. 4.8. The

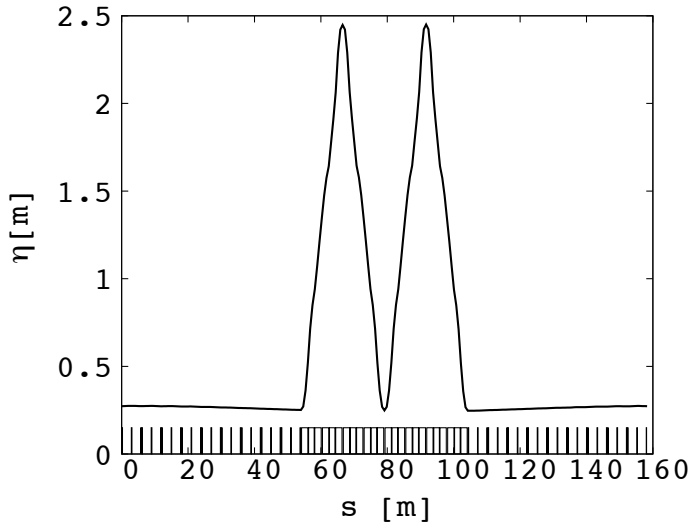

Figure 4.8: Dispersion function for p_0 in half of the ring. The plot is centered on the arc part.

ring tune point is (5.30, 2.52) at p_0. Stability of the ring tune has been studied over the momentum range. The tune variation is kept within 0.1 both in horizontal and vertical, and is presented in the tune diagram in Fig. 4.9. Beta-functions of p_0, p_{min}, and p_{max} are plotted in Fig. 4.10.

Acceptance study at fixed energy (3.6 GeV and 12.6 GeV) has been done, and maximum stable amplitude over 100 turns are presented in Fig. 4.11.

Multi particle has then been conducted, with a beam composed of 1000 particles. These particles are uniformly distributed at 2 GeV (kinetic energy) $\pm 16\%$ in momentum and then uniformly distributed inside a transverse 4D ellipsoid (Waterbag distribution). The emittance is 400 π mm.mrad unnormalized both in horizontal and vertical. The initial beam distribution in the phase spaces is shown in Fig. 4.12. The particles do 60 turns, i.e. about their lifetime. The results show that 6.9% of the particles are lost in the lattice

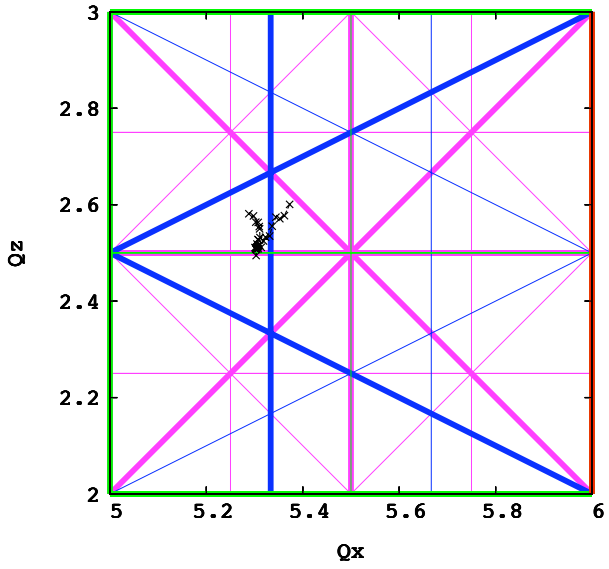

Figure 4.9: Ring tunes for muons from p_{min} to p_{max} ($\pm$16% in momentum around 2.1 GeV/c). Integer (red), half-integer (green), third integer (blue) and fourth integer (purple) normal resonances are plotted. Structural resonances are in bold.

(see Fig. 4.12). The horizontal and vertical Poincaré map of the beam after the 60 turns are presented in Fig. 4.13. The distribution in horizontal angle of the particles is shown in Fig. 4.14.

The momentum range is limited by the dispersion mismatch between the straight part and the arc part. A better dispersion matching could improve it. Multi particle tracking has been done, and 6.9% of the particles are lost in the simulation. The tune working point crosses the horizontal third-integer resonance and is very close to the vertical fourth-integer resonance. A better choice of the working point could decrease the number of lost particles.

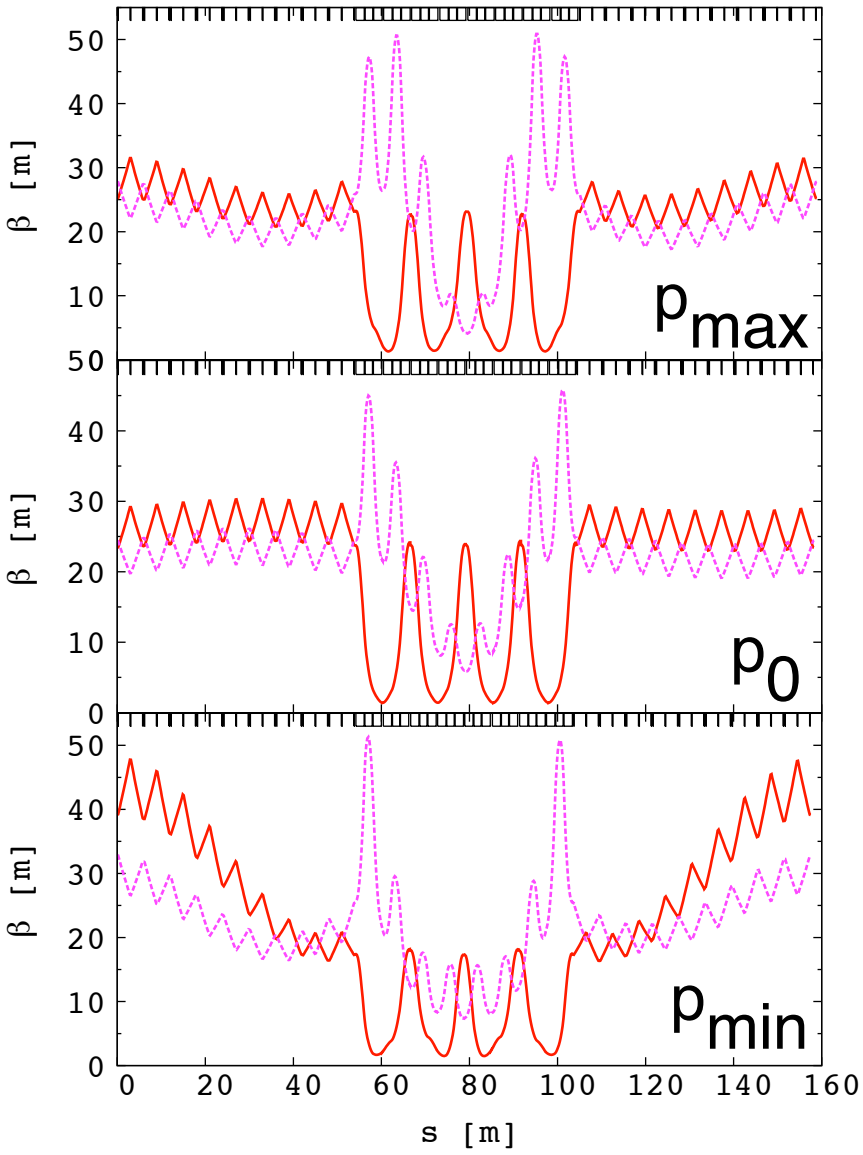

Figure 4.10: Horizontal (plain red) and vertical (dotted purple) periodic beta-functions of half of the VLENF racetrack ring for p_{max} (top scheme), p_0 (middle scheme), and p_{min} (bottom scheme). The plot is centered on the arc part.

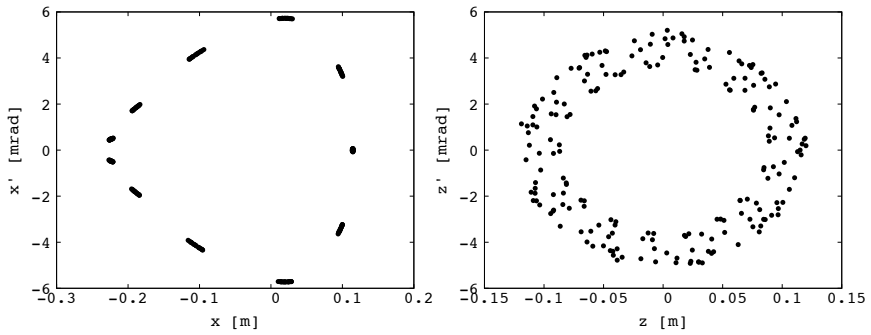

Figure 4.11: Horizontal (left) and vertical (right) Poincaré map showing the maximum amplitude for a stable motion over 100 turns for p_0.

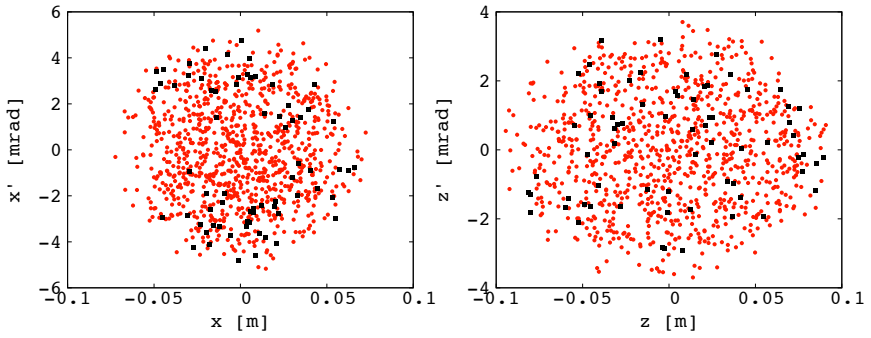

Figure 4.12: Horizontal (left) and vertical (right) Poincaré maps showing the particle distribution at the beginning of the simulation in red circles ($\sim$400 π mm.mrad unnormalized emittance). The black squares indicate the injected particles lost during the simulation.

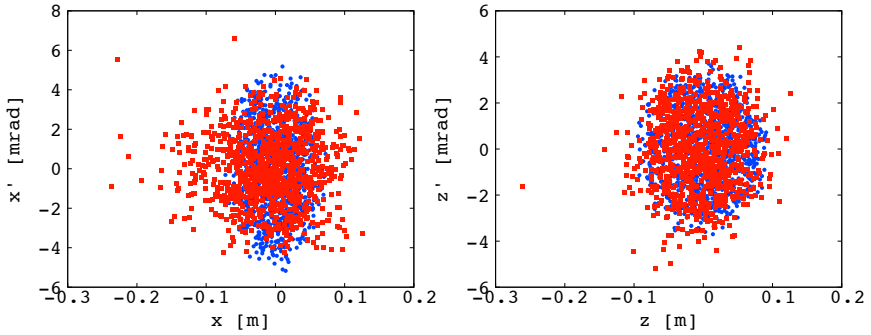

Figure 4.13: Horizontal (left) and vertical (right) Poincaré maps showing the particle distribution at the injection (blue circles) and at the end of the simulation (red squares).

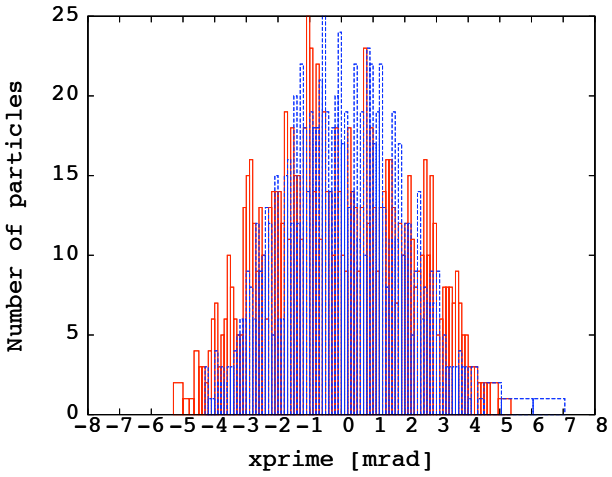

Figure 4.14: Horizontal distribution in angle of the injected beam (plain red), and at the end of the simulation (dotted blue).

4.3 Long drift space for injection and extraction

4.3.1 Muon phase rotator in PRISM

The PRISM (Phase Rotated Intense Slow Muon beam) project aims to realize a low-energy muon beam with a high-intensity, narrow energy spread and high purity. A layout is presented in Fig. 4.15, where a scaling FFAG ring has been proposed as a phase rotator [32]. Requirements for the FFAG ring include a very large transverse and longitudinal acceptance. The original design of the FFAG ring for PRISM is based on 10 identical DFD triplets. If this design fulfills the requirements of acceptance, the excursion is very large and the injection and extraction still remains difficult. Further work is now gathered in the PRISM task force [33].

	Circular Section	Straight Section
Type	FDF	FDF
Cell radius [m]/opening angle [deg] or Length [m]	2.7/30	1.8
k-value or m-value	2.6	1.3 m^{-1}
Horizontal phase advance /cell [deg]	60	27
Vertical phase advance /cell [deg]	90	97
Average dispersion /cell [m]	0.8	0.8
Number of cells /ring	6×2	6×2

Table 4.3: Parameters of the racetrack PRISM lattice.

4.3.2 A modular system with long straight sections

Race-track FFAG ring

To solve the problem of injection and extraction, we consider the use of straight cells in the lattice and a new design is proposed (see Fig. 4.16). Parameters are summarized in table 4.3. The beta-functions for a momentum

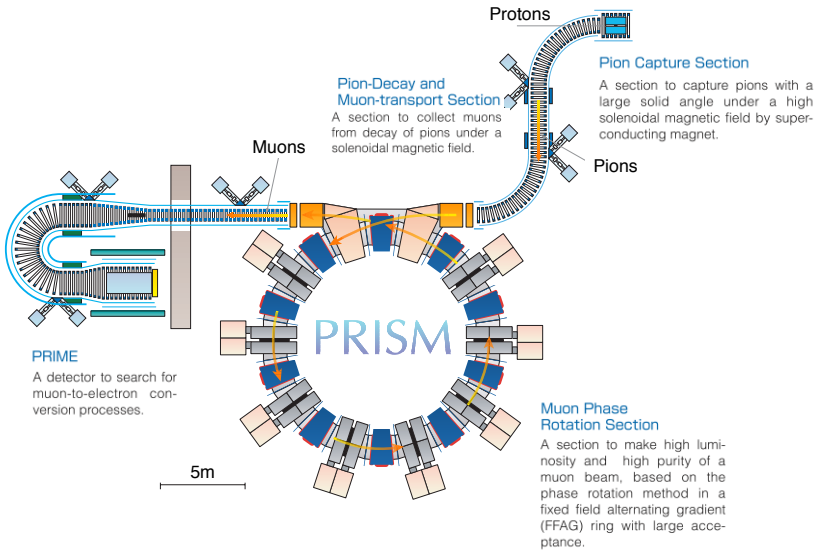

Figure 4.15: Layout of the PRISM project. The detector PRIME (PRISM muon to electron) to study the muon to electron events is also presented on the left part.

of 68 MeV/c are presented in Fig. 4.17. The working point is chosen in the tune diagram so that it is far from the structural normal resonances. The present working point has a tune of 2.9 in horizontal and 6.3 in vertical. The transverse acceptance in both planes is studied by tracking over 50 turns. Horizontal ($\sim 24,\ 000$ π.mm.mrad) and vertical ($\sim 6,\ 000$ π.mm.mrad) acceptances are then measured (see Fig. 4.18).

Egg-shape FFAG ring

An other design incorporating arc sections with different radii, "egg-shaped", gives also more drift spaces for injection and extraction (see Fig. 4.19). Parameters are summarized in Table 4.4. The beta-functions for a momentum of 68 MeV/c are presented in Fig. 4.17. The working point is chosen in the tune diagram so that it is far from the structural normal resonances. The present working point has a tune of 2.9 in horizontal and 6.3 in vertical, and is constant over the momentum range.

4.4 Low-vertical beta function insertion

4.4.1 Emittance/energy recovery internal target

The ERIT (Energy/Emittance Recovery Internal Target) project with a scaling type of FFAG proton storage ring has been proposed as an accelerator-based intense thermal or epithermal neutron source (ABNS) for boron neu-

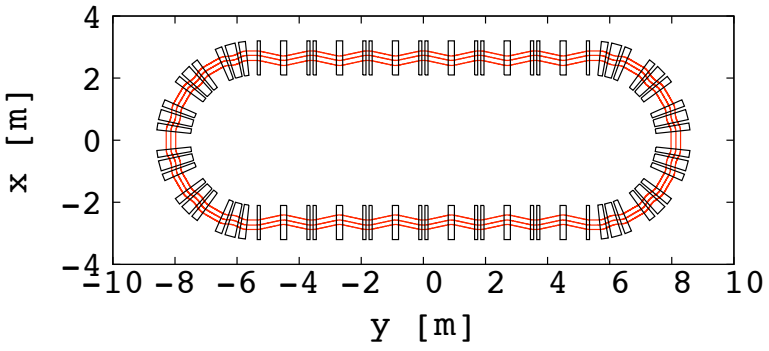

Figure 4.16: Closed orbits of 55 MeV/c, 68 MeV/c and 82 MeV/c muons μ^- in the PRISM lattice with straight sections.

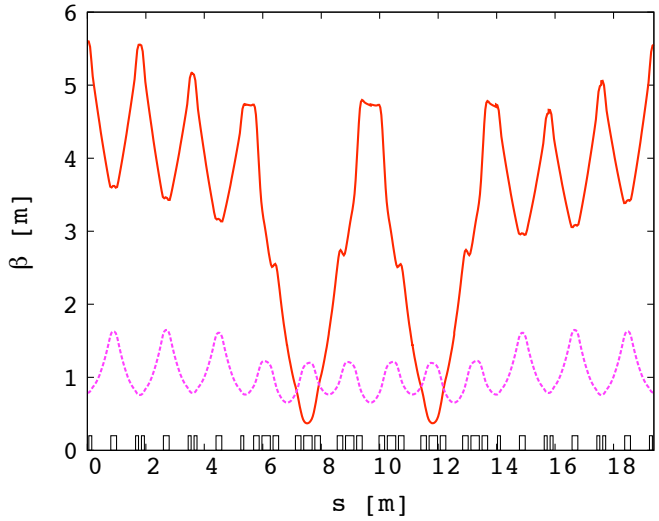

Figure 4.17: Horizontal (plain red) and vertical (dotted purple) beta-functions for half of the ring of the PRISM lattice. The plot is centered on the arc part.

tron capture therapy and constructed in Kyoto University Research Reactor Institute [30]. Emittance blow up due to multiple scattering and energy straggling in the target is limited by ionization cooling.

The results are promising [31], but since limitation of the survival rate of the protons comes from the emittance growth in the vertical plane, an insertion with a minimum of vertical beta-function could improve this scheme.

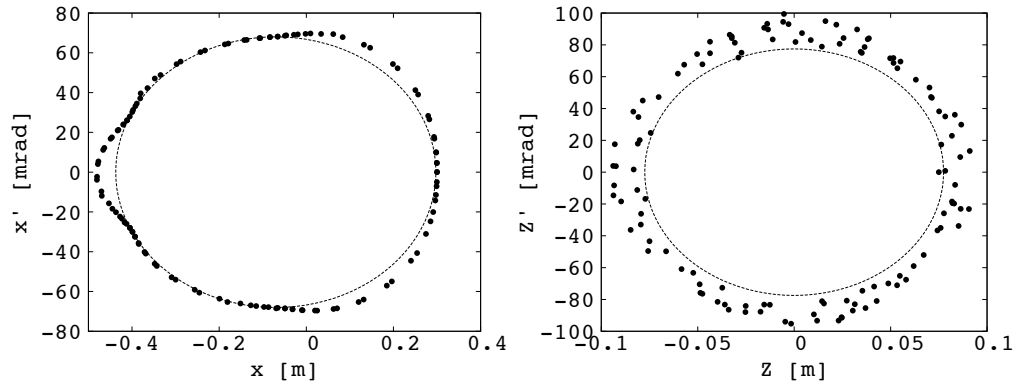

Figure 4.18: Horizontal (left) and vertical (right) Poincaré map showing the maximum amplitude for a stable motion over 50 turns for 68 MeV/c in the racetrack PRISM lattice.

	Large radius Section	**Small radius Section**
Type	FDF	FDF
Cell opening angle [deg]	11.70	39.15
k-value	29.0	3.82
Radius [m]	30	5
Horizontal phase advance [deg]	74.7	90.0
Vertical phase advance [deg]	80.8	60.0
Average dispersion [m]	1.0	1.0
Number of cells in the ring	2×2	4×2

Table 4.4: Parameters of the egg-shape PRISM lattice.

4.4.2 Low-vertical beta function insertion

The purpose of the insertion is to decrease the value of the vertical beta-function at the target. In the existing scheme, the vertical beta-function is 0.8 m. The length of the insertion is settled from the RF frequency of the existing cavity (18.2 MHz). To minimize the effect of the mismatch on the

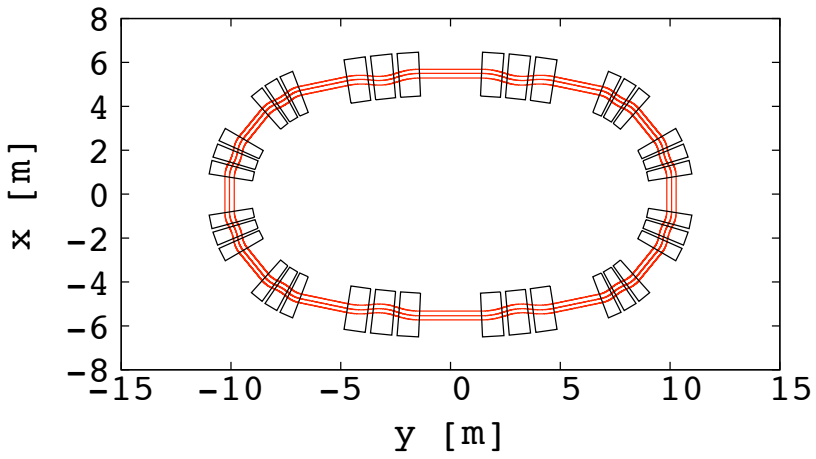

Figure 4.19: Closed orbits of 55 MeV/c, 68 MeV/c and 82 MeV/c muons μ^- in the egg-shape PRISM lattice.

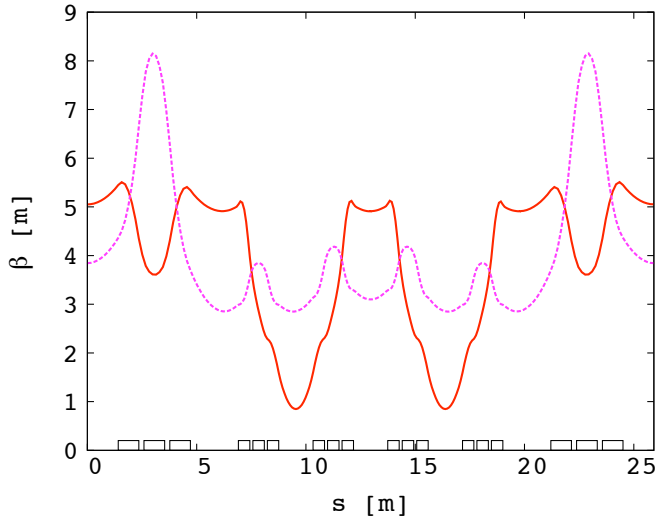

Figure 4.20: Horizontal (plain red) and vertical (dotted purple) beta-functions for half of the ring of the PRISM egg-shape lattice.

amplitude of the betatron oscillations, the arc is modified by changing the k-value (from 1.92 to 2.57) to become transparent. This change in the design will have a small effect on dispersion (from 0.8 m to 0.65 m). The parameters of the new lattice are presented in table 4.5.

Particle tracking is done again with Runge-Kutta integration in the same conditions than in the PRISM case. The tune is 2.22 in horizontal and 2.82 in vertical.

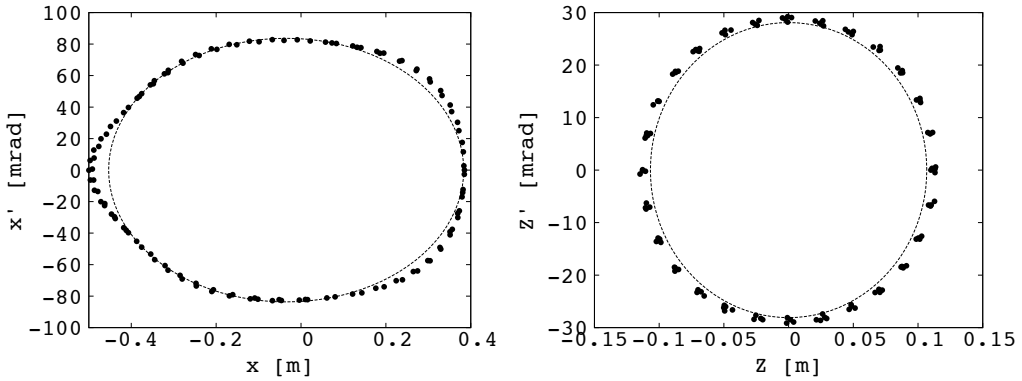

Figure 4.21: Horizontal (left) and vertical (right) Poincaré map showing the maximum amplitude for a stable motion over 50 turns for 68 MeV/c in the egg-shape PRISM lattice.

	Circular Section	**Straight Section**
Type	FDF	DFFD
Cell radius [m]/opening angle [deg] or Length [m]	2.35/45	1.40
k-value or m-value	2.57	$1.52\,\mathrm{m}^{-1}$
Horizontal phase advance /cell [deg]	90	41
Vertical phase advance /cell [deg]	90	148
Average dispersion /cell [m]	0.66	0.66
Number of cells /ring	4×2	1×2

Table 4.5: Parameters of the new ERIT lattice.

Beta-functions are presented in Fig. 4.23). At the target, the horizontal beta-function is 3.2 m and the vertical one 0.29 m. The vertical beta-function is thus smaller by a factor of 3 at the target, but the horizontal one is bigger by a factor of 2.5 compared with the original lattice. Further study must be realized to check if the horizontal acceptance (more than 8500 π mm.mrad, see Fig. 4.24) is enough to handle the overheating due to the increase of the beta-function.

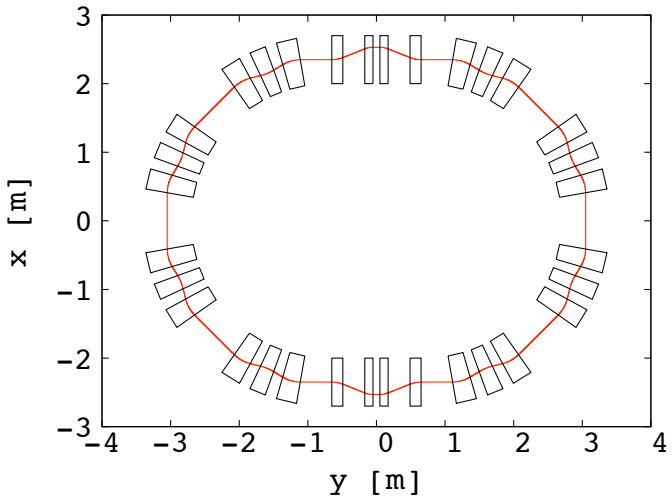

Figure 4.22: Closed orbit of 11 MeV proton in the ERIT lattice with the insertion.

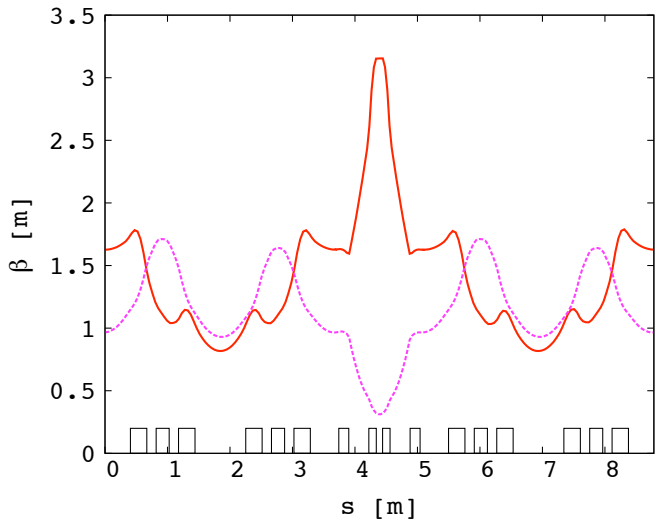

Figure 4.23: Horizontal (plain red) and vertical (dotted purple) beta-functions for half of the ring of the ERIT lattice.

4.5 Zero-chromatic FFAG transport lines

4.5.1 Transport lines for beams with large momentum spread

Beams with large momentum spread are usually guided by solenoids, but it is of a very weak focusing and requires large magnetic field, since there is

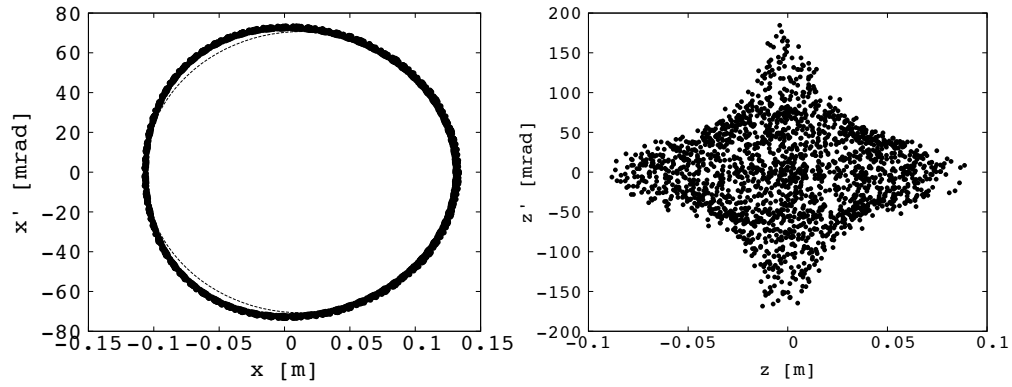

Figure 4.24: Horizontal (left) and vertical (right) Poincaré map showing the maximum amplitude for a stable motion over 1000 turns for 11 MeV proton in the ERIT lattice.

no field at the center of the solenoids. Zero-chromatic FFAG transport lines would then be an improvement, giving strong focusing to the system.

4.5.2 Gantries for hadrontherapy

FFAG transport line could be useful to transport different momenta in a short time in the same line, like in hadron therapy gantries. In zero-chromatic FFAGs, each momentum has a different reference trajectory. Dispersion suppressors are then necessary at the beginning and at the end of the gantry since all different momenta come from and arrive at the same point. Another constraint comes from the reverse bend in the line. It induces to reverse the dispersion between the two bends, or to use a negative-k lattice in one of the

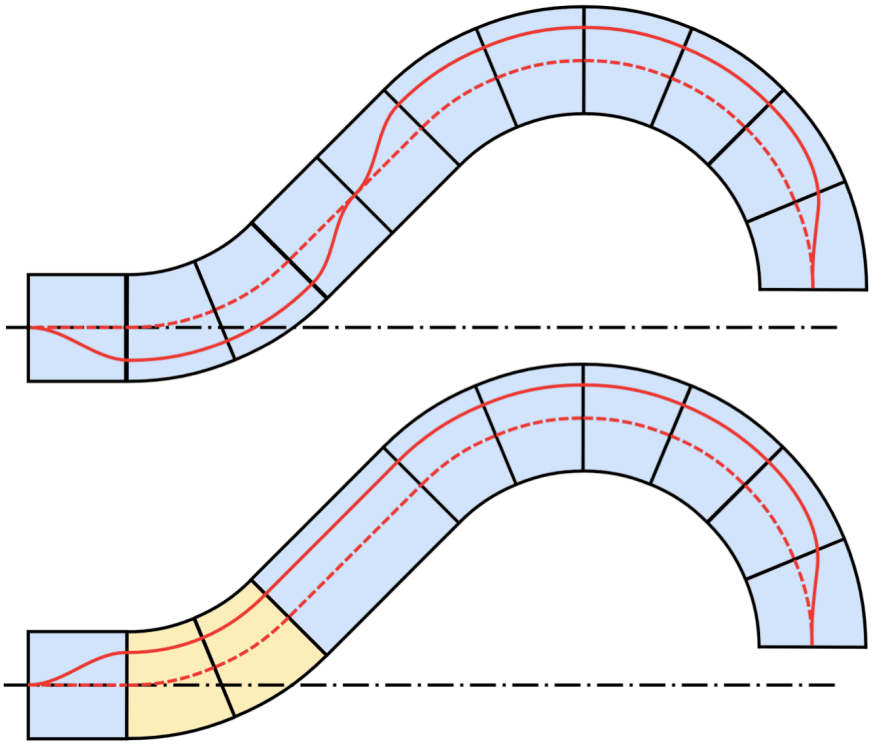

Figure 4.25: Schematic layout of a zero-chromatic FFAG gantry. The dotted red line represents the trajectory of a middle momentum, and the plain red line the maximum momentum. The mixed lines represents the rotation axis. The upper scheme shows the case of a reverse dispersion, the lower one the case of a negative-k lattice (in yellow).

bends. A schematic layout is presented in Fig. 4.25.

Chapter 5
Summary

In chapter 1, historical background of FFAG accelerators are first presented. Imagined first by Ohkawa in 1953 [2], the principle of this type of particle accelerator has been successfully demonstrated in America in the 60s. No significant improvement followed during the four next decades, but new needs and new available technological tools favored the rebirth of FFAGs.

Basic features of particle accelerator physics are then introduced, with the introduction of betatron oscillations around a closed orbit, leading to the notion of chromaticity, defined as the variation of the number of these oscillations per turn with energy. The importance of keeping the zero-chromaticity is then briefly developed. Avoiding betatron resonance crossing is indeed a key feature in particle physics.

The purpose of the study is finally presented. FFAG accelerators usually suppress the chromaticity with a particular magnetic field configuration, called "scaling" law because of the scaling property of the orbit geometry. But this field law constrains the transverse motion and ring shape, with few free parameters for lattice design. The goal of the study is then to provide more flexibility in lattice design for this kind of accelerator, with the development of straight zero-chromatic FFAG lines.

In chapter 2, the theoretical approach is expounded, with the analytical development of the invariance of the betatron oscillations with momentum in circular FFAG, leading to the scaling law. The orbit similarity must be fulfilled, and the magnetic field configuration in the mid-plane follows

$$B_z = B_{0z} \left(\frac{r}{r_0} \right)^k \cdot \mathcal{F}, \tag{5.1}$$

with r the polar coordinate, k the constant geometrical field index, $\mathcal{F}$ an arbitrary function and $B_{0z} = B_z(r_0)$.

The same approach is then applied to the straight case, leading to another condition for the invariance of the betatron oscillations, that we call "straight scaling" law. Like in the circular case, the orbit similarity must be fulfilled, but the magnetic field configuration in the mid-plane follows

$$B_z = B_{0z} e^{m(x-x_0)} \mathcal{F},$$

with x the horizontal cartesian coordinate, m the constant normalized field gradient, $\mathcal{F}$ an arbitrary function and $B_{0z} = B_z(x_0)$.

The combination of different scaling FFAG cells is then discussed, with the central notion of cell dispersion function introduced. By matching this cell dispersion function around an arbitrary momentum, any shape can be obtained for the FFAG accelerator. This matching is done to the first order and higher orders create a mismatch for the reference trajectories that can degrade the zero-chromaticity condition if the momentum range is too large.

These considerations lead to the dispersion suppressor principle, where scaling FFAG cells with different cell dispersion η_1 and η_3 could be matched with a π-phase-advance insertion, made of scaling FFAG cells itself, and with the cell dispersion η_2 following

$$\eta_2 = \frac{\eta_1 + \eta_3}{2}. \tag{5.2}$$

This principle is based on the linear theory, and higher orders can degrade the zero-chromaticity condition for a large momentum range. One solution to overcome this difficulty is to use several insertions in cascade to change progressively the dispersion.

In chapter 3, the straight scaling FFAG experiment is developed. The apparatus is first presented, with the use of 11 MeV and 7 MeV H^- beam from the linac injector of the FFAG complex in KURRI. This beam is collimated by two aligned collimators, to set the Courant-Snyder parameters at the entrance of the straight scaling FFAG cell prototype. A beam emittance measurement system composed of a movable slit, a fluorescent screen and a camera is installed after the straight cell to measure the exit parameters. Design of the cell prototype is then presented, with tracking first in field model to adjust the parameters, then magnet pole shape is designed with POISSON and TOSCA. Tracking in TOSCA 3D field map is

then done to optimize the pole shape, field clamp configuration and current density in the coils. The magnets are then manufactured. Field of the magnets has been measured, and tracking in the created field maps has been done. The agreement with TOSCA field map tracking is within 1%, which is in the acceptable range. The phase advance has been measured, and a difference of 1.6% between 11 MeV and 7 MeV has been calculated. The agreement is good with tracking, since the difference is less than 1% for 11 MeV and around 2% for 7 MeV. This experiment validates the straight scaling FFAG law. Concerning the error bars, they are quite large, especially for 7 MeV, because of the incident beam fluctuations, and are inevitable.

In chapter 4, applications of the new theory are presented. Reduced excursions insertions for rf cavities are investigated. An example with the acceleration of relativistic muon beams with the so-called harmonic number jump scheme for neutrino factories is then developed.

Zero-chromatic race-track FFAG rings become also a possibility. A muon decay ring for very low energy neutrino factory is designed as an example.

Modular lattices are then introduced with the example of two designs to allow injection and extraction in the PRISM FFAG phase rotator. The first one is a race-track lattice with long straight sections, the second one is "egg-shape" lattice composed of circular sections with different radii. Both designs fulfill the requirements of transverse acceptance.

Dedicated insertions are then presented, with the particular example of a low-vertical-beta insertion to improve the ERIT scheme.

Zero-chromatic transport lines are finally introduced to handle large momentum spread beams. FFAG gantries for hadrontherapy are also briefly introduced.

Chapter 6
Conclusion

The aim of this study is to give more freedom in lattice design for zero-chromatic FFAG accelerators. It is based on a new magnetic field configuration to guide particles with no overall bend, while keeping the zero-chromaticity, i.e. the invariance of the focusing strength with energy.

The historical background and general features of FFAG accelerators have first briefly been described. This type of particle accelerator fell into disuse after the sixties, but is subject to a recent regained interest due to its unique characteristics. FFAGs can reach relativistic energies, contrary to cyclotrons, and fixed field leaves them free from magnet ramping issues, by contrast of pulsed synchrotrons. New demands for accelerators have indeed risen these days in physics and in medical field, especially in high beam power, and new technologies and computation tools have allowed this rebirth of FFAGs.

Chromaticity parameter has been then introduced. It is an essential parameter in particle accelerators. It creates indeed issues of betatron resonance crossing, and limits the momentum range available in the machine.

An analytical development of the invariance of the betatron oscillations with momentum in circular FFAG leads to the "scaling law". It is possible to keep the transverse linearized equations of motion independent of momentum if two conditions are fulfilled. The first one is that the different momentum closed orbits should be photographic enlargements from each other in the median plane, and the second one is that the vertical magnetic field in the median plane follows a law in machine radius to the power of k, constant geometrical field index. The corresponding development for the straight FFAG is then exposed. It leads to a different magnetic field configuration than in circular elements. It is indeed possible to keep the transverse linearized equations of motion independent of momentum if two equivalent conditions to the circular case are fulfilled. The first one is the orbit similarity, that is to say the different momentum reference trajectories are a translation of each other in the median plane, and the second one is the vertical magnetic

field Bz in the median plane should follow the "straight scaling" law

$$B_z = B_{0z} e^{m(x-x_0)} \mathcal{F},$$

with x the horizontal cartesian coordinate, m the normalized field gradient, $\mathcal{F}$ an arbitrary function and $B_{0z} = B_z(x_0)$.

Theoretical applications have also been presented, especially the introduction of insertions in FFAG accelerators. Different scaling FFAG cells can actually be combined by matching the dispersion around a central momentum. A dispersion suppressor principle to reduce the excursion of the beam is then developed.

To study this new field law, the world's first experiment on straight scaling FFAG has been done at Kyoto University Research reactor Institute. A prototype of a FFAG cell with this particular magnetic field configuration has been designed and manufactured, and the magnetic field measured. Phase advances of two different energies passing through this prototype cell are quantified, and their difference is 1.6%. This difference is acceptable, regarding the precision of the measurement. The agreement with tracking results is also good, since the difference is in the 2% range. The experimental results thus concur with the theory and confirm the straight scaling law.

Practical applications of this discovery have then been investigated. Reduced excursion insertions where rf cavities can be installed can improve the efficiency of the acceleration. A muon FFAG racetrack decay ring for neutrino factories with a large momentum spread becomes possible. In the PRISM project, the FFAG ring used as a phase rotator can have more space for injection and extraction. The ionization cooling in vertical in the ERIT system can be improved with a low vertical beta function insertion. Transport lines for large momentum spread beams and FFAG gantries for hadrontherapy are finally a practical possibility.

This original work thus opens a new area for FFAG accelerators, that we call "advanced scaling FFAG" , with a new range of applications. It gives an answer to a wide range of unsolved problems until now. It gives also a better understanding of the zero-chromaticity condition in FFAGs. The flexibility in FFAG synchrotrons lattice design has been improved very much, with a modular system similar to conventional synchrotrons. Further steps require an experiment on dispersion suppressor principle, which could be done with an upgrade of the straight scaling FFAG experiment done at KURRI.

Appendix A

Betatron oscillations and non linear beam dynamics

The motion of a particle of momentum p around a closed orbit is described by the following linearized equations of motion for small amplitudes

$$\begin{cases} \dfrac{\mathrm{d}^2x}{\mathrm{d}s^2} + \dfrac{1}{\rho^2}(1-n)\cdot x = 0, & \text{(a)} \\ \dfrac{\mathrm{d}^2z}{\mathrm{d}s^2} + \dfrac{n}{\rho^2}\cdot z = 0\,, & \text{(b)} \end{cases} \tag{A.1}$$

with s the longitudinal coordinate along the closed orbit, x and z, the horizontal and vertical transverse coordinates, respectively, and ρ the local radius of curvature of the closed orbit. The field index n is defined as:

$$n = -\frac{\rho}{B}\left(\frac{\partial B}{\partial x}\right)_{\perp}, \tag{A.2}$$

with B the vertical component of the magnetic field. The symbol $\perp$ means that the partial derivative is done in the machine mid-plane perpendicularly to the closed orbit, and evaluated at $x = 0$. The parameters ρ and n are periodic functions of s, since particle orbits are closed. The linearized equations of motion Eq. A.1(a) and Eq. A.1(b) are then of the form of Hill's equations.

In the following development, we use the subscript notations of a parameter A, A_x and A_z, to distinguish the horizontal and vertical components of this parameter, respectively. The general solutions of Eq. A.1(a) and Eq. A.1(b) are of the form [53]

$$\begin{cases} x = a_x\sqrt{\beta_x(s)}\cos(\nu_x\phi_x(s) + \phi_{0x}), \\ z = a_z\sqrt{\beta_z(s)}\cos(\nu_z\phi_z(s) + \phi_{0z}), \end{cases} \tag{A.3}$$

with a and ϕ_0 arbitrary constants, and β the periodic Courant-Snyder beta-function. The betatron cell tune ν is defined as

$$\nu = \frac{1}{2\pi}\int\frac{\mathrm{d}s}{\beta}, \tag{A.4}$$

and the phase $\phi(s)$ is given by

$$\phi(s) = \int \frac{\mathrm{d}s}{\nu\beta}. \tag{A.5}$$

The motion of particles described by Eq. A.3 can be seen as a pseudo-harmonic oscillation so-called betatron oscillation around the equilibrium orbit, characterized by its frequency ν and its varying amplitude following the square root of the beta-function β. The notation Q represents the ring tune and is defined as:

$$Q = N\nu, \tag{A.6}$$

with N the ring periodicity. The definition of the betatron tune leads to the related notion of chromaticity, defined as the variation of the tune with respect to the momentum of the particles.

Except in the rare case where magnetic field is linear, field configuration gives rise to non-linear field components. These non-linear components are usually considered as perturbation terms of Eq. A.1 in beam dynamics studies. It leads to the related notion of resonance condition, whose general expression is [54, 55]

$$m_x Q_x + m_z Q_z = q, \tag{A.7}$$

where m_x, m_y and q are small integers. When the tune (Q_x, Q_z) is close to such a resonance condition, the amplitude of the betatron oscillation can increase, generating emittance degradation and even beam losses.

Appendix B

Step-wise tracking simulation code

During this study a step-wise tracking simulation code has been developed to study lattice parameters and 6D beam dynamics in FFAG accelerators. It is written in C language. In this section we describe the basic principles of this simulation code.

B.1 Particle tracking in static magnetic fields

We first of all consider the motion of a charged particle in a static magnetic field. In this case, since the magnetic force does not work, the total momentum p of the particle is invariant. The effect of electric fields coming from rf cavities is considered later (in Sec. B.3). The exact equations of motion express in cartesian coordinates (x, y, z) can thus be written as:

$$\begin{cases} \dfrac{\mathrm{d}u_x}{\mathrm{d}s} = \dfrac{(u_y B_z - u_z B_y)}{B\rho} \\ \dfrac{\mathrm{d}u_y}{\mathrm{d}s} = \dfrac{(u_z B_x - u_x B_z)}{B\rho} \\ \dfrac{\mathrm{d}u_z}{\mathrm{d}s} = \dfrac{(u_x B_y - u_y B_x)}{B\rho} \\ \dfrac{\mathrm{d}x}{\mathrm{d}s} = u_x \\ \dfrac{\mathrm{d}y}{\mathrm{d}s} = u_y \\ \dfrac{\mathrm{d}z}{\mathrm{d}s} = u_z \end{cases} , \tag{B.1}$$

where s is the longitudinal abscissa measured along the orbit of the particle, and $B\rho$ is the magnetic rigidity of the particle, also given by:

$$B\rho = \frac{p}{q}, \tag{B.2}$$

with q the charge of the particle. The magnetic field is $\vec{B}$ =(B_x, B_y, B_z), and $\vec{u}$ =(u_x, u_y, u_z) is a unit vector defined as:

$$\vec{u} = \frac{\vec{p}}{p}. \tag{B.3}$$

B.1.1 Analytical field modeling

To compute the trajectory of a particle, we need a description of the magnetic field produced by the scaling type of FFAG magnets. We choose to use analytical field models similar to those used in the 'FFAG' procedure of the tracking code Zgoubi, and described in Ref. [56].

We start by modeling the field distribution in the machine mid-plane. Since it is an anti-symmetry plane of the field distribution, only the vertical component B_z of the magnetic field may exist along this plane.

Circular case

In the case of circular type of FFAG cells, it is convenient to describe the field distribution in the mid-plane using the polar coordinates (r, θ). The contribution of each magnet is obtained following the equation:

$$B_z(r,\theta) = B_0\,\mathcal{F}(\theta)\,\left(\frac{r}{r_0}\right)^k, \tag{B.4}$$

where $B_0 = B_z(r_0,\theta)$. The function $\mathcal{F}(\theta)$ describes the azimuthal variation of the field, and does not depend on r. In the linear field fall-off approximation, the function $\mathcal{F}(\theta)$ can be written as

$$\begin{cases} \mathcal{F} = \dfrac{\theta - \Theta_{EFB_{en}} + \Theta_{FE_{en}}}{2\Theta_{FE_{en}}}, \text{ for } \Theta_{EFB_{en}} - \Theta_{FE_{en}} \leq \theta < \Theta_{EFB_{en}} + \Theta_{FE_{en}} \\ \mathcal{F} = 1, \text{ for } \Theta_{EFB_{en}} + \Theta_{FE_{en}} \leq \theta < \Theta_{EFB_{ex}} - \Theta_{FE_{ex}} \\ \mathcal{F} = 1 - \dfrac{\theta - \Theta_{EFB_{ex}} + \Theta_{FE_{ex}}}{2\Theta_{FE_{ex}}}, \text{ for } \Theta_{EFB_{en}} + \Theta_{FE_{en}} \leq \theta < \Theta_{EFB_{ex}} - \Theta_{FE_{ex}} \\ \mathcal{F} = 0, \text{ for } \theta < \Theta_{EFB_{en}} - \Theta_{FE_{en}} \text{ or } \theta \geq \Theta_{EFB_{ex}} - \Theta_{FE_{ex}}, \end{cases} \tag{B.5}$$

with $\Theta_{EFB_{en}}$ and $\Theta_{EFB_{ex}}$ the effective field boundary azimuths at the entrance and at the exit, respectively, and $\Theta_{FE_{en}}$ and $\Theta_{FE_{ex}}$ the fringe field extent azimuths at the entrance and at the exit, respectively. We use the

Maxwell's equations to obtain the field components off the mid-plane. We thus consider the Taylor expansion of the field around the mid-plane:

$$B_u(r,\theta,z) = B_u(r,\theta,0) + \sum_{i=1}^{\infty} \frac{z^i}{i!} \frac{\partial^i B_u}{\partial z^i}\,, \tag{B.6}$$

with u standing for either r, θ or z, partial derivatives being taken at $z = 0$. Since the machine mid-plane is an anti-symmetry plane of the field distribution, we can write that:

$$\begin{aligned} B_r(r,\theta,0) &= 0 \\ B_\theta(r,\theta,0) &= 0 \\ B_r(r,\theta,-z) &= -B_r(r,\theta,z) \\ B_\theta(r,\theta,-z) &= -B_\theta(r,\theta,z) \\ B_z(r,\theta,-z) &= B_z(r,\theta,z) \end{aligned} \tag{B.7}$$

The Taylor expansion thus simplifies to:

$$\begin{aligned} B_r(r,\theta,z) &= z\frac{\partial B_r}{\partial z} + O(z^3) \\ B_\theta(r,\theta,z) &= z\frac{\partial B_\theta}{\partial z} + O(z^3) \\ B_z(r,\theta,z) &= B_0 + O(z^2) \end{aligned} \tag{B.8}$$

To express the partial derivatives used in the Taylor expansion as a function of the partial derivatives we can easily get from Eq. B.4, we use the Maxwell's equations. From the Maxwell-Ampère equation one gets:

$$\begin{aligned} \frac{\partial B_r}{\partial z} &= \frac{\partial B_z}{\partial r} && \text{(a)} \\ \frac{\partial B_\theta}{\partial z} &= \frac{1}{r}\frac{\partial B_z \theta}{\partial \theta} && \text{(b)} \\ \frac{\partial B_r}{\partial \theta} &= \frac{\partial B_\theta}{\partial r} && \text{(c)} \end{aligned} \quad . \tag{B.9}$$

From Eqs. B.9(a) and B.9(b), we get the first order terms in Eq. B.8. The magnetic field components at an arbitrary position (r, θ, z) of the cell is obtained summing the contribution of each magnet of the cell. Finally we move from cylindrical to cartesian coordinates by a change of variables.

We have thus described the principle used for the analytical field modeling. The detailed formula are shown below in the subroutine used to compute and add the field contribution of each FFAG magnet:

```
extern void add_field_comp_FFAGradial_lin(double x, double y, double z, double *bx, ↩
     double *by, double *bz, struct Cell *cell, int ic)
{
    double r, th, ffbe, ffbs, r0, k, bz0, thfringe_e, thfringe_s, br, bth, bz_peak, ↩
         bz_local;

    //convert cartesian local framework coordinates into cylindrical
    r = sqrt(x*x + y*y);
    th = atan_ratio(y, x);

    //use component parameters
    ffbe = cell->mpara[ic][0] + cell->efben[ic][0]; //[rad]
    ffbs = cell->mpara[ic][0] + cell->efbex[ic][0]; //[rad]
    r0 = cell->mpara[ic][1];
    bz0 = cell->mpara[ic][2];
    k = cell->mpara[ic][3];
    thfringe_e = cell->efben[ic][1]; //[rad]
    thfringe_s = cell->efbex[ic][1]; //[rad]

    br = 0;
    bth = 0;
    bz_local = 0;
    bz_peak = bz0*pow(r/r0, k);

    if(ffbs - ffbe < thfringe_e + thfringe_s) printf("!Warning in ↩
         add_field_comp_FFAGradial_lin: magnet length < thfringe_e + thfringe_s !\n");

    //compute br, bth, bz
    if(thfringe_e != 0 && th >= ffbe - thfringe_e && th < ffbe + thfringe_e) {
        bz_local = bz_peak*((th - ffbe + thfringe_e)/(2.*thfringe_e));
        br = z/r*k*bz_local;
        bth = z/r*bz_peak/(2.*thfringe_e);
    }
    else if(th >= ffbe + thfringe_e && th <= ffbs - thfringe_s) {
        bz_local = bz_peak;
        br = z/r*k*bz_local;
        bth = 0;
    }
    else if(thfringe_s != 0 && th > ffbs - thfringe_s && th <= ffbs + thfringe_s) {
        bz_local = bz_peak*(1 - (th - ffbs + thfringe_s)/(2.*thfringe_s));
        br = z/r*k*bz_local;
        bth = -z/r*bz_peak/(2.*thfringe_s);
    }

    //add contribution of this component onto the bfield in the Cell (components of b ↩
         field in the local cartesian framework)
    *bx += br*cos(th) - bth*sin(th);
    *by += bth*cos(th) + br*sin(th);
    *bz += bz_local;
}
```

Straight case

In the case of straight type of FFAG cells, the field distribution in the mid-plane is described using the cartesian coordinates (x, y). The contribution of each magnet is obtained following the equation:

$$B_z(x, y) = B_0 \, \mathcal{F}(y) \, e^{m(x - x_0)}, \tag{B.10}$$

where $B_0 = B_z(x_0, y)$. The function $\mathcal{F}(y)$ describes the longitudinal variation of the field, and does not depend on x. In the linear field fall-off

approximation, the function $\mathcal{F}(y)$ can be written as

$$\begin{cases} \mathcal{F} = \dfrac{y - Y_{EFB_{en}} + Y_{FE_{en}}}{2Y_{FE_{en}}}, \text{ for } Y_{EFB_{en}} - Y_{FE_{en}} \leq y < Y_{EFB_{en}} + Y_{FE_{en}} \\ \mathcal{F} = 1, \text{ for } Y_{EFB_{en}} + Y_{FE_{en}} \leq y < Y_{EFB_{ex}} - Y_{FE_{ex}} \\ \mathcal{F} = 1 - \dfrac{y - Y_{EFB_{ex}} + Y_{FE_{ex}}}{2Y_{FE_{ex}}}, \text{ for } Y_{EFB_{en}} + Y_{FE_{en}} \leq y < Y_{EFB_{ex}} - Y_{FE_{ex}} \\ \mathcal{F} = 0, \text{ for } y < Y_{EFB_{en}} - Y_{FE_{en}} \text{ or } y \geq Y_{EFB_{ex}} - Y_{FE_{ex}}, \end{cases} \tag{B.11}$$

with $Y_{EFB_{en}}$ and $Y_{EFB_{ex}}$ the effective field boundary abscissa at the entrance and at the exit, respectively, and $Y_{FE_{en}}$ and $Y_{FE_{ex}}$ the fringe field extent abscissa at the entrance and at the exit, respectively. We use the Maxwell's equations to obtain the field components off the mid-plane. We thus consider the Taylor expansion of the field around the mid-plane:

$$B_u(x, y, z) = B_u(x, y, 0) + \sum_{i=1}^{\infty} \frac{z^i}{i!} \frac{\partial^i B_u}{\partial z^i}\,, \tag{B.12}$$

with u standing for either x, y or z, partial derivatives being taken at $z = 0$. Since the machine mid-plane is an anti-symmetry plane of the field distribution, we can write that:

$$\begin{aligned} B_x(x, y, 0) &= 0 \\ B_y(x, y, 0) &= 0 \\ B_x(x, y, -z) &= -B_x(x, y, z) \\ B_y(x, y, -z) &= -B_y(x, y, z) \\ B_z(x, y, -z) &= B_z(x, y, z) \end{aligned} \tag{B.13}$$

The Taylor expansion thus simplifies to:

$$\begin{aligned} B_x(x, y, z) &= z\frac{\partial B_x}{\partial z} + O(z^3) \\ B_y(x, y, z) &= z\frac{\partial B_y}{\partial z} + O(z^3) \\ B_z(x, y, z) &= B_0 + O(z^2) \end{aligned} \tag{B.14}$$

To express the partial derivatives used in the Taylor expansion as a function of the partial derivatives we can easily get from Eq. B.4, we use the Maxwell's

equations. From the Maxwell-Ampère equation one gets:

$$\begin{aligned} \frac{\partial B_x}{\partial z} &= \frac{\partial B_z}{\partial x} \quad \text{(a)} \\ \frac{\partial B_y}{\partial z} &= \frac{\partial B_z}{\partial y} \quad \text{(b)} \\ \frac{\partial B_x}{\partial y} &= \frac{\partial B_y}{\partial x} \quad \text{(c)} \end{aligned} \quad . \tag{B.15}$$

From Eqs. B.15(a) and B.15(b), we get the first order terms in Eq. B.8. The magnetic field components at an arbitrary position (r, θ, z) of the cell is obtained adding the contribution of each magnet of the cell.

We have thus described the principle used for the analytical field modeling. The detailed formula are shown below in the subroutine used to compute and add the field contribution of each FFAG magnet:

```
extern void add_field_comp_FFAGstraight_lin(double x, double y, double z, double *bx, ↩
     double *by, double *bz, struct Cell *cell, int ic)
{
    double bz_peak, bz_local, ffbe, ffbs, x0, bz0, m, lambda_e, lambda_s;

    //use component parameters
    ffbe = cell->mpara[ic][0] + cell->efben[ic][0];
    ffbs = cell->mpara[ic][0] + cell->efbex[ic][0];
    x0 = cell->mpara[ic][1];
    bz0 = cell->mpara[ic][2];
    m = cell->mpara[ic][3];
    lambda_e = cell->efben[ic][1];
    lambda_s = cell->efbex[ic][1];

    bz_peak = bz0*exp(m*(x - x0));

    if(ffbs - ffbe < lambda_e + lambda_s) printf("!Warning in add_field_onemagnet_lin:↩
         magnet length < lambda_e + lambda_s !\n");

    if(lambda_e != 0 && y >= ffbe - lambda_e && y < ffbe + lambda_e) {
        bz_local = bz_peak*((y - ffbe + lambda_e)/(2.*lambda_e));
        *bx += z*bz_local*m;
        *by += z*bz_peak/(2.*lambda_e);
        *bz += bz_local;
    }
    else if(y >= ffbe + lambda_e && y <= ffbs - lambda_s) {
        bz_local = bz_peak;
        *bx += z*bz_local*m;
        *by += 0;
        *bz += bz_local;
    }
    else if(lambda_s != 0 && y > ffbs - lambda_s && y <= ffbs + lambda_s) {
        bz_local = bz_peak*(1 - (y - ffbs + lambda_s)/(2.*lambda_s));
        *bx += z*bz_local*m;
        *by += -z*bz_peak/(2.*lambda_s);
        *bz += bz_local;
    }
}
```

B.1.2 Integration of the equations of motion

Numerical integration is used with the given 3D field distribution to solve step-by-step the equations of motion (Eq. B.1). To that end we use standard 4^{th} order Runge-Kutta integration algorithms (see Ref. [57]). Such integrators are widely used in many fields of research since they provide a high level of precision compared to the computation time. They moreover do not require to specify a reference orbit around which the motion is integrated, by contrast to symplectic integrators. This is an essential feature for simulating acceleration in the case of FFAGs, in which the closed orbit moves during acceleration.

However, the main drawback of such integrators is that the errors coming from the truncated terms, although very small for each step, can be accumulated over a large number of steps, which may lead to artificial non-symplectic behaviors.

For the standard code Zgoubi (which is also non-necessarily symplectic) as for the code developed at Kyoto University, a careful use is required. Not bounded trajectories in the transverse phase spaces may come from either a resonant behavior or a problem of symplecticity. Distinction between these two effects can be done by launching the same simulation with a different step-size.

B.2 Calculation of the linear parameters

If we neglect the effect of non-linear field components, the particle motion with respect to its closed orbit can be described in either the horizontal of the vertical planes by means of linear transfer matrices:

$$\begin{pmatrix} y_1 \\ y'_1 \end{pmatrix} = \begin{pmatrix} a_{11} & a_{12} \\ a_{21} & a_{22} \end{pmatrix} = \begin{pmatrix} y_0 \\ y'_0 \end{pmatrix}, \tag{B.16}$$

where y stands either for x or z. To determine such transfer matrices, we track five particles with initial positions as described in Fig. B.1.

Taking into account non-linear forces, the positions of these particle after

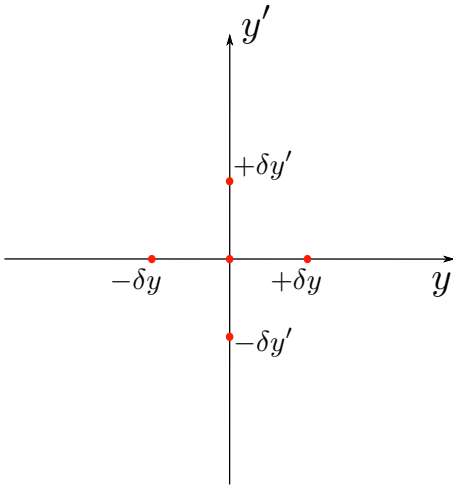

Figure B.1: Initial position in a transverse phase space (either horizontal or vertical) of the five particles used to compute the equivalent linear transfer matrix. The notation δy represents a small displacement perpendicularly to the closed orbit, while the notation $\delta y'$ represents a small angular deviation with respect to the closed orbit.

tracking can be written as:

$$\begin{aligned}
y_{+\delta y} &= a_{11}\delta y + b_{11}\delta y^2 + O(\delta y^3) \\
y_{-\delta y} &= -a_{11}\delta y + b_{11}\delta y^2 + O(\delta y^3) \\
y'_{+\delta y} &= a_{21}\delta y + b_{21}\delta y^2 + O(\delta y^3) \\
y'_{-\delta y} &= -a_{21}\delta y + b_{21}\delta y^2 + O(\delta y^3) \\
y_{+\delta y'} &= a_{12}\delta y' + b_{12}\delta y'^2 + O(\delta y'^3) \\
y_{-\delta y'} &= -a_{12}\delta y' + b_{12}\delta y'^2 + O(\delta y'^3) \\
y'_{+\delta y'} &= a_{22}\delta y' + b_{22}\delta y'^2 + O(\delta y'^3) \\
y'_{-\delta y'} &= -a_{22}\delta y' + b_{22}\delta y'^2 + O(\delta y'^3)
\end{aligned} \tag{B.17}$$

Here again the distance are measures perpendicularly to the closed orbit.

The linear matrix coefficients is thus be determined as:

$$\begin{aligned} a_{11} &= \frac{y_{+\delta y} - y_{-\delta y}}{2\delta y} + O(\delta y^3) \\ a_{12} &= \frac{y'_{+\delta y} - y'_{-\delta y}}{2\delta y} + O(\delta y^3) \\ a_{21} &= \frac{y_{+\delta y'} - y_{-\delta y'}}{2\delta y'} + O(\delta y'^3) \\ a_{22} &= \frac{y'_{+\delta y'} - y'_{-\delta y'}}{2\delta y'} + O(\delta y'^3) \end{aligned} \tag{B.18}$$

This way the contribution of the second order terms is thus cancelled out with this method. Values for δy and $\delta y'$ are chosen small (typically 0.1 mm and 0.1 mrad), so that the truncation error $O(\delta y^3)$ is negligible.

Once the equivalent transfer matrix between two arbitrary points of the lattice can be obtained, it is straightforward to get the values linear tunes tunes, as well as phase advances and periodic Courant Snyder-parameters all along the lattice.

B.3 Acceleration: effect of the rf field

We simulate the effect of thin rf gaps by incrementing the kinetic energy of the particle of qV_{rf}, with q the charge of the particle, and the rf gap voltage V_{rf} is given by:

$$V_{rf} = V_0 \sin(2\pi f_{rf} t + \phi_0), \tag{B.19}$$

where the cavity peak voltage V_0, the rf frequency f_{rf}, and the initial phase ϕ_0 are kept unchanged during acceleration. It is thus necessary to know the time of flight t of the particle. This required to integrate an additional differential equation:

$$\frac{\mathrm{d}t}{\mathrm{d}s} = \frac{\gamma}{c(\gamma^2 - 1)}, \tag{B.20}$$

where c is the speed of light and γ is the Lorentz factor of the particle. While only the knowledge of the particle rigidity ($B\rho$) was enough to solve the equation of motion without acceleration (Eq. B.1), we need here to know also the particle rest mass m_0 and charge q to be able to determine its Lorentz factor since:

$$\gamma = \sqrt{1 + \left(\frac{qB\rho}{m_0 c}\right)^2}. \tag{B.21}$$

Bibliography

[1] E. D. Courant, M. S. Livingston, H. S. Snyder, The strong-focusing synchroton—a new high energy accelerator, Phys. Rev. 88 (5) (1952) 1190–1196. doi:10.1103/PhysRev.88.1190.

[2] T. Ohkawa, in: Symposium on Nuclear Physics of the Physics Society of Japan, 1953, y. Mori, private communication.

[3] A.A. Kolomensky, V.A. Petukhov and M.S. Rabinovich, Some problems in the theory of cyclic accelerators, Academy of Sciences of the USSR, Moscow, 1955, p. 7.

[4] K. R. Symon, D. W. Kerst, L. W. Jones, L. J. Laslett, K. M. Terwilliger, Fixed-field alternating-gradient particle accelerators, Phys. Rev. 103 (6) (1956) 1837–1859. doi:10.1103/PhysRev.103.1837.

[5] F. T. Cole, O CAMELOT! A memoir of the MURA years, (section 6.1), april 1994, published in: Proc. Cycl. Conf., 2001.
URL http://cern.ch/AccelConf/c01/cyc2001/extra/Cole.pdf

[6] F. T. Cole, R. O. Haxby, L. W. Jones, C. H. Pruett, and K. M. Terwilliger, Electron model fixed field alternating gradient accelerator, Rev. Sci. Instrum. 28 (6) (1957) 403–420. doi:10.1063/1.1715895.

[7] D. W. Kerst, *et al.*, Fixed field alternating gradient accelerators with spirally ridged poles, Phys. Rev. 98 (4) (1955) 1153, in: Minutes of the Meeting of the Division of Fluid Dynamics, Virginia, November, 1954, p. 1153. doi:10.1103/PhysRev.98.1139.

[8] D. W. Kerst, E. A. Day, H. J. Hausman, R. O. Haxby, L. J. Laslett, F. E. Mills, T. Ohkawa, F. L. Peterson, E. M. Rowe, A. M. Sessler, J. N. Snyder, and W. A. Wallenmeyer, Electron model of a spiral sector accelerator, Rev. Sci. Instrum. 31 (10) (1960) 1076–1106. doi:10.1063/1.1716818.

[9] F. T. Cole, G. Parzen, C. H. Pruett, W. A. Wallenmeyer, and D. E. Young, MURA 50-MeV electron accelerator general description and review, Rev. Sci. Instrum. 35 (11) (1964) 1393–1397. doi:10.1063/1.1719171.

[10] C. M. Ankenbrandt, M. Atac, B. Autin, V. I. Balbekov, V. D. Barger, O. Benary, J. S. Berg, M. S. Berger, E. L. Black, A. Blondel, S. A. Bogacz, T. Bolton, S. Caspi, C. Celata, W. Chou, D. B. Cline, J. Corlett, L. Cremaldi, H. T. Diehl, A. Drozhdin, R. C. Fernow, D. A. Finley, Y. Fukui, M. A. Furman, T. Gabriel, J. C. Gallardo, A. A. Garren, Status of muon collider research and development and future plans, Phys. Rev. ST Accel. Beams 2 (8) (1999) 081001. doi:10.1103/PhysRevSTAB.2.081001.

[11] S. Geer, Neutrino beams from muon storage rings: Characteristics and physics potential, Phys. Rev. D 57 (11) (1998) 6989–6997. doi:10.1103/PhysRevD.57.6989.

[12] Y. Mori, Advancement of the scaling ffag accelerator for adsr, pulsed-sns and muon acceleration, International Journal of Modern Physics A 26 (10 and 11) (2011) 1744–1752. doi:10.1142/S0217751X11053146.

[13] Y, Mori, Ffag proton driver for muon source, Nuclear Instruments and Methods in Physics Research Section A: Accelerators, Spectrometers, Detectors and Associated Equipment 451 (1) (2000) 300 – 303. doi:10.1016/S0168-9002(00)00555-6.
URL http://www.sciencedirect.com/science/article/pii/S0168900200005556

[14] Y. Mori, FFAG accelerators and their applications, in: Proceedings of EPAC'06 Conference, Edinburgh, UK, 2006, pp. 950–954.

[15] S. Antoine, B. Autin, W. Beeckman, J. Collot, M. Conjat, F. Forest, J. Fourrier, E. Froidefond, J.L. Lancelot, J. Mandrillon, P. Mandrillon, F. Méot, Y. Mori, D. Neuvéglise, C. Ohmori, J. Pasternak and T. Planche, Principle design of a protontherapy, rapid-cycling, variable energy spiral FFAG, Nucl. Instr. and Meth. A 602 (2) (2009) 293 – 305. doi:10.1016/j.nima.2009.01.025.

[16] K. Peach, *et al.*, PAMELA - a model for an FFAG based hadron therapy machine, in: Proc. of PAC'07 Conf., 2007, pp. 2880–2882.

[17] Vector Fields Ltd., TOSCA OPERA-3D reference manual.

[18] M. Aiba, *et al.*, A 150MeV FFAG synchrotron with "return-yoke free" magnet, in: Proc. of PAC'01 Conf., 2001, pp. 3254–3256.

[19] K. Okabe, T. Uesugi, Y. Kuriyama, T. Planche, J.-B. Lagrange, Y. Ishi, I. Sakai, Y. Mori, Design and construction of FFAG magnets for the ERIT system at KURRI, Applied Superconductivity, IEEE Transactions on 20 (3) (2010) 740–743. doi:10.1109/TASC.2010.2042696.

[20] T. Planche, J. Fourrier, J.L. Lancelot, F. Méot, D. Neuvéglise and J. Pasternak, Design of a prototype gap shaping spiral dipole for a variable energy protontherapy FFAG, Nucl. Instr. and Meth. A 604 (3) (2009) 435 – 442. doi:10.1016/j.nima.2009.02.026.

[21] F. Méot, The ray-tracing code zgoubi, Nucl. Instr. and Meth. A 427 (1-2) (1999) 353 – 356. doi:10.1016/S0168-9002(98)01508-3.

[22] M. Aiba and F. Méot, Determination of KEK 150 MeV FFAG parameters from ray-tracing in TOSCA eld maps, Tech. Rep. CEA DAPNIA-04-188, CERN-NUFACT-Note-140, CEA DAPNIA (Oct. 2004).
URL http://cdsweb.cern.ch/record/806545

[23] T. Planche, E. Yamakawa, T. Uesugi, J.-B. Lagrange, Y. Kuriyama, K. Okabe, Y. Ishi, Y. Mori, Scaling FFAG rings for rapid acceleration of muon beams, Nucl. Instr. and Meth. A 622 (1) (2010) 21 – 27. doi:10.1016/j.nima.2010.06.242.

[24] C. Ohmori, *et al.*, A wideband RF cavity for JHF synchrotrons, in: Proc. of PAC'97 Conf., Vol. 3, 1997, pp. 2995–2997. doi:10.1109/PAC.1997.753086.

[25] I. Bolotin, *et al.*, Ferromagnetic cores made from amorphous material for broad-band accelerating system, in: Proc. of PAC'95 Conf., Vol. 3, 1995, pp. 1833 –1834. doi:10.1109/PAC.1995.505377.

[26] A. Sato, *et al.*, Development of a FFAG proton synchrotron, in: Proc. of EPAC'00 Conf., 2000, pp. 581–583.

[27] S, Machida, *et al.*, Commissioning of 150MeV FFAG synchrotron, in: Proc. of EPAC'04 Conf., 2004, pp. 2643–2645.

[28] C. H. Pyeon, T. Misawa, J-Y. Lim, H Unesaki, Y. ishi, Y Kuriyama, T. Uesugi, Y. Mori, M. Inoue, K. Nakajima, K. Mishima, and S. Shiroya, First injection of spallation neutrons generated by high-energy protons into the Kyoto University Critical Assembly, J. Nucl. Sci. Tech. 46 (12) (2009) 1091–1093. doi:10.3327/jnst.46.1091.

[29] Y. Kuno, Y. Mori, and the NufactJ Working Group, A feasibility study of a neutrino factory in Japan, v. 1.0 (2001).
URL http://www-prism.kek.jp/nufactj/nufactj.pdf

[30] Y. Mori, Development of FFAG accelerators and their applications for intense secondary particle production, Nucl. Instr. and Meth. A 562 (2) (2006) 591 – 595. doi:10.1016/j.nima.2006.02.044.

[31] K. Okabe, *et al.*, An intense neutron source with emittance recovery internal target (ERIT) using ionization cooling, in: Proc. of EPAC'08 Conf., 2008, pp. 3512–3514.

[32] K. Yoshimura, Prism overview, Nucl. Instr. and Meth. A 503 (1-2) (2003) 254 – 257. doi:10.1016/S0168-9002(03)00688-0.

[33] J. Pasternak, *et al.*, Accelerator and particle physics research for the next generation muon to electron conversion experiment - the PRISM task force, in: Proc. of IPAC'10 Conf., 2010, pp. 3473–3475.

[34] J. Pasternak, Recent studies on the prism ffag ring, IOP Conference Proceedings (2011) To be published.

[35] J. Berg, Recent results from optimization studies of linear non-scaling FFAGs for muon acceleration, in: S. Machida, Y. Mori, and T. Yokoi (Ed.), Proc. of FFAG'04 conference, Osaka, Japan, 2004, pp. 1–8.
URL http://hadron.kek.jp/FFAG/FFAG04_HP/

[36] R. Barlow, J. Berg, C. Beard, N. Bliss, J. Clarke, M. Craddock, J. Crisp, R. Edgecock, Y. Giboudot, P. Goudket, S. Griffiths, C. Hill, S. Jamison, C. Johnstone, A. Kalinin, E. Keil, D. Kelliher, S. Koscielniak, S. Machida, K. Marinov, N. Marks, B. Martlew, P. McIntosh, F. Méot, A. Moss, B. Muratori, H. Owen, Y. Rao, Y. Saveliev, S. Sheehy, B. Shepherd, R. Smith, S. Smith, S. Tzenov, A. Wheelhouse, C. White, T. Yokoi, Emma? the world's first non-scaling ffag, Nuclear Instruments and Methods in Physics Research Section A: Accelerators, Spectrometers, Detectors and Associated Equipment 624 (1) (2010) 1 – 19. doi:10.1016/j.nima.2010.08.109.
URL http://www.sciencedirect.com/science/article/pii/S0168900210018978

[37] S. Machida, Emma, recent developments, IOP Conference Proceedings (2011) To be published.

[38] C. Johnstone, M. Berz, K. Makino, S. Koscielniak, P. Snopok, Advances in nonlinear non-scaling ffags, International Journal of Modern Physics A 26 (10 and 11) (2011) 1690–1712. doi:10.1142/S0217751X11053110.

[39] P. F. Meads, A dispersion-free long straight section for a fixed-field alternating-gradient synchrotron, Nuclear Science, IEEE Transactions on 30 (4) (1983) 2448 –2450. doi:10.1109/TNS.1983.4332843.

[40] P. F. Meads, A compensated dispersion-free long insertion for an FFAG synchrotron, in: Proceedings of the Particle Accelerator Conference 1993, 1993, pp. 3825–3827 vol.5. doi:10.1109/PAC.1993.309814.

[41] J.-B. lagrange, T. Planche, Y. Mori, Zero-chromatic ffag straight section, International Journal of Modern Physics A 26 (10 and 11) (2011) 1785–1793. doi:10.1142/S0217751X11053183.

[42] J.-B. Lagrange, T. Planche, Y. Mori, Scaling ffag accelerator for muon acceleration, AIP Conference Proceedings 1382 (1) (2011) 234–236. doi:10.1063/1.3644321.
URL http://link.aip.org/link/?APC/1382/234/1

[43] J. Lagrange, T. Planche, E. Yamakawa, Y. Ishi, Y. Kuriyama, Y. Mori, B. Qin, T. Uesugi, K. Okabe, A. Sardet, R. Wasef, Straight scaling ffag line, IOP Conference Proceedings (2011) To be published.

[44] J.-B. Lagrange, T. Planche, E. Yamakawa, T. Uesugi, Y. Ishi, Y. Kuriyama, B. Qin, K. Okabe, Y. Mori, Straight scaling FFAG beam line, Nucl. Instr. and Meth. A to be published.

[45] P. Fork, Beam instrumentation and diagnostics.

[46] POISSON/SUPERFISH reference manual, Los Alamos National Laboratory, 1987.
URL http://books.google.co.jp/books?id=YZL2GwAACAAJ

[47] B. Qin, Y. Mori, Compact superferric ffag accelerators for medium energy hadron applications, Nuclear Instruments and Methods in Physics Research Section A: Accelerators, Spectrometers, Detectors and Associated Equipment 648 (1) (2011) 28 – 34. doi:10.1016/j.nima.2011.05.035.
URL http://www.sciencedirect.com/science/article/pii/S0168900211009429

[48] The ISS Accelerator Working Group, *et al.*, Accelerator design concept for future neutrino facilities, J. Instr. 4 (2009) P07001. doi:10.1088/1748-0221/4/07/P07001.

[49] T. Planche, J.-B. Lagrange, E. Yamakawa, T. Uesugi, Y. Kuriyama, K. Okabe, Y. Ishi, Y. Mori, Harmonic number jump acceleration of muon beams in zero-chromatic ffag rings, Nuclear Instruments and Methods in Physics Research Section A: Accelerators, Spectrometers, Detectors and Associated Equipment 632 (1) (2011) 7 – 17. doi:10.1016/j.nima.2010.12.190.
URL http://www.sciencedirect.com/science/article/pii/S016890021002992X

[50] T. Planche, Study of zero-chromatic ffag synchrotron for muon acceleration, PhD dissertation, Kyoto University (2010).

[51] C. Giunti, M. Laveder, W. Winter, Short-baseline electron neutrino disappearance at a neutrino factory, Phys. Rev. D 80 (2009) 073005.

doi:10.1103/PhysRevD.80.073005.
URL http://link.aps.org/doi/10.1103/PhysRevD.80.073005

[52] A. Bross, The very low energy neutrino factory, neutrino physics with a muon storage ring, IOP Conference Proceedings (2011) To be published.

[53] E. D. Courant, H. S. Snyder, Theory of the alternating-gradient synchrotron,, Annals of Physics 3 (1) (1958) 1 – 48. doi:DOI:10.1016/0003-4916(58)90012-5.

[54] G. Guignard, A general treatment of resonances in accelerators, Tech. Rep. 78-11, CERN, lecture given in the Academic Training Programme of CERN 1977-1978 (Nov. 1978).

[55] R. D. Ruth, Single particle dynamics in circular accelerators, Tech. Rep. SLAC-PUB-4103, SLAC, Stanford University, Stanford, CA 94305 (Oct. 1986).

[56] F. Lemuet, F. Méot, Developments in the ray-tracing code Zgoubi for 6-D multiturn tracking in FFAG rings, Nucl. Instr. and Meth. A 547 (2-3) (2005) 638 – 651. doi:10.1016/j.nima.2005.03.156.

[57] W.H. Press, S.A. Teukolsky, W.T. Vetterling, and B.P. Flannery, Numerical Recipies in C, 2nd Edition, Cambridge University Press, Reading, Massachusetts, 1992, Ch. 16.
URL http://www.nrbook.com/a/bookcpdf.php

List of reviewed publications

Related to the Chapter 2

J.-B. Lagrange, T. Planche and Y. Mori, International Journal of Modern Physics A, vol. 26, numbers 10-11, pp. 1785-1793, zero-chromatic FFAG straight section.

J.-B. Lagrange, T. Planche and Y. Mori, AIP conference Proceedings, 1382, 234 (2011), scaling FFAG accelerator for muon acceleration.

J.-B. Lagrange, T. Planche, E. Yamakawa, Y. Ishi, Y. Kuriyama, Y. Mori, B. Qin, T. Uesugi and Kota Okabe, Nuclear Instruments and Methods in Physics Research Section A, Straight scaling FFAG beam line, submitted.

Related to the Chapter 3

J.-B. Lagrange, T. Planche, E. Yamakawa, Y. Ishi, Y. Kuriyama, Y. Mori, B. Qin, T. Uesugi, Kota Okabe, A. Sardet and R. Wasef, IOP conference proceedings, straight scaling FFAG line, submitted.

J.-B. Lagrange, T. Planche, E. Yamakawa, Y. Ishi, Y. Kuriyama, Y. Mori, B. Qin, T. Uesugi and Kota Okabe, Nuclear Instruments and Methods in Physics Research Section A, Straight scaling FFAG beam line, submitted.

Related to the Chapter 4

J.-B. Lagrange, T. Planche and Y. Mori, AIP conference Proceedings, 1382, 234 (2011), scaling FFAG accelerator for muon acceleration.

T. Planche and J.-B. Lagrange and E. Yamakawa and T. Uesugi and Y. Kuriyama and K. Okabe and Y. Ishi and Y. Mori, Nuclear Instruments and Methods in Physics Research Section A, vol. 632, number 1, pp. 7-17, Harmonic number jump acceleration, 2011.

T. Planche and E. Yamakawa and T. Uesugi and J.-B. Lagrange and Y. Kuriyama and K. Okabe and Y. Ishi and Y. Mori, Nuclear Instruments and Methods in Physics Research Section A, vol 622, number 1, pp. 21-27, Scaling FFAG rings for rapid acceleration of muon beams, 2010.

K. Okabe, T. Uesugi, Y. Kuriyama, T. Planche, J.-B. Lagrange, Y. Ishi, I. Sakai, Y. Mori, IEEE Transactions on applied superconductivity, vol. 20, number 3, pp. 740-743, Design and Construction of FFAG Magnets for the ERIT System at KURRI, 2010.